



Influence of spanwise wall vibration on non-modal perturbations subject to freestream vortical disturbances in hypersonic boundary layers

Qinyang Song¹, Ming Dong^{1,†}, Lei Zhao^{2,†}, Xianying Chu³ and Ningning Wu³

¹State Key Laboratory of Nonlinear Mechanics, Institute of Mechanics, Chinese Academy of Sciences, Beijing 100190, PR China

²Department of Mechanics, Tianjin University, Tianjin 300072, PR China

³Beijing Aerospace Technology Institute, Beijing 100074, PR China

(Received 13 January 2024; revised 19 August 2024; accepted 26 September 2024)

In this paper, we study the effect of lateral wall vibrations on the excitation and evolution of non-modal perturbations in hypersonic boundary layers subject to low-frequency freestream vortical disturbances (FSVDs). A novel, high-efficiency numerical approach, combining the harmonic weakly nonlinear Navier–Stokes and nonlinear parabolised stability equation approaches, is developed, which is sufficient to accommodate both the rapid distortion of the perturbation in the leading-edge vicinity and the nonlinear development of finite-amplitude high-order harmonics in the downstream region. The boundary-layer response to low-frequency FSVDs shows a longitudinal streaky structure, for which the temperature perturbation shows much greater magnitude than the streamwise velocity perturbation. The lateral vibration induces a Stokes layer solution for the spanwise velocity perturbation, which interacts with the FSVD-induced perturbations and leads to a suppression of the non-modal perturbation and an enhancement of the downstream modal perturbation. The new perturbations excited by the FSVD–vibration interaction strengthen as the vibration intensifies, and they could become comparable with the FSVD-induced perturbations in downstream locations at a high vibration intensity, indicating a remarkable modification of the streaky structure and its instability property. Secondary instability (SI) analyses based on the streaky base flow indicate that the vibration could enhance or suppress the SI modes, depending on their initial phases over the vibration period. Overall, the average effect is that the low-frequency and high-frequency SI modes are stabilised and destabilised by the vibration, respectively. Since the high-frequency SI modes undergo higher amplifications, the subsequent bypass transition is likely to be promoted by relatively strong vibrations.

† Email addresses for correspondence: dongming@imech.ac.cn, lei_zhao@tju.edu.cn

Key words: boundary layer stability, transition to turbulence

1. Introduction

Accurate predictions of the aerodynamic performance are usually the first task of the design of high-speed flying vehicles, which are severely influenced by the laminar–turbulent transition because the drag and heat flux undergo drastic increase during the transition process (Zhong & Wang 2012). For low environmental perturbations, the boundary-layer transition follows a natural route, for which the receptivity, linear instability, nonlinear interaction of the normal instability mode and turbulence appear in sequence (Kachanov 1994; Wu 2019). As reviewed by Mack (1987), there exist a multitude of instability modes in hypersonic boundary layers, which are referred to as the Mack first, second and high-order modes, and the second mode is more unstable. The traditional method to predict the natural transition is based on the accumulated growth of the linear instability modes, referred to as the e-N method (Smith 1956), which, however, often provides unsatisfactory predictions due to its exclusion of the receptivity process, the effect of surface imperfections, and the nonlinear instability mechanisms. Much attention has been paid to these issues in the recent years. The theoretical descriptions of the hypersonic receptivity mechanism include the leading-edge receptivity (Fedorov & Khokhlov 2001; Goldstein & Ricco 2018), the local receptivity (Dong, Liu & Wu 2020; Zhao, He & Dong 2023), and the receptivity at the neutral point as an optimal excitation (Qin & Wu 2016; Hernández & Wu 2019). For hypersonic boundary layers with blunt noses, the receptivity efficiency, including the impacts of the bow-shaped shock and entropy layer, was studied by direct numerical simulations (DNS) (Wan, Su & Chen 2020; Niu & Su 2023). The impacts of local roughness elements and thermal sources on the Mack instability evolution were formulated by Dong & Zhao (2021) and Zhao & Dong (2022), respectively. The mechanism of fundamental resonance in hypersonic boundary layers was observed numerically by Hader & Fasel (2019), and subsequently formulated using the asymptotic technique by Song, Dong & Zhao (2024). A comprehensive review of the nonlinear instability theory can be found in Wu (2019).

When the intensity of the freestream perturbations is moderate, the transition may occur bypassing the appearance of normal instability modes, referred to as the bypass transition. Characterising the freestream vortical disturbances (FSVDs) and their entrainment into the boundary layer is a crucial issue describing the bypass transition process. In the incompressible regime and for relatively weak FSVDs, the mathematical theory for entrainment was formulated by Leib, Wundrow & Goldstein (1999), who showed that long-wavelength (low-frequency) FSVDs generate streaks, and the latter were governed by linear boundary-region equations together with appropriate initial and boundary conditions. The theory was extended by Ricco, Luo & Wu (2011) to the more realistic case of strong FSVDs, where nonlinear boundary-region equations describe the generation and evolution of streaks. The streaks do not break down themselves, but they could support the amplification of the high-frequency perturbations due to the secondary instability (SI) mechanism (Andersson *et al.* 2001; Ricco *et al.* 2011; Xu, Zhang & Wu 2017). These modes would eventually cause the emergence of the turbulent spots (Wu, Moin & Hickey 2014; Wu 2023), and their excitation by high-frequency FSVDs was studied by Zhang, Dong & Zhang (2018). Simulations for the bypass transition by extending the computational domain to include the region upstream of the leading edge can be found in Nagarajan, Lele & Ferziger (2007) and Ovchinnikov, Choudhari & Piomelli (2008).

The theory for excitation of streaks by FSVDs in compressible flows was formulated by Ricco & Wu (2007) and Marensi, Ricco & Wu (2017), using the linear and nonlinear boundary-region equations, respectively. Theoretical studies of the bypass transition in hypersonic boundary layers are quite insufficient, and the major difficulty is attributed to the impact of the shock wave forming in the leading-edge vicinity, which, however, could be overcome by numerics. Recently, numerical calculations of the optimal growth of non-modal perturbations in blunt-cone hypersonic boundary layers were conducted by Paredes *et al.* (2019*a,b*). It was found that the amplification rate of the optimal non-modal perturbations increases with the radius of the nose tip, and the bypass transition may appear if the nose radius is over a threshold. A subsequent analysis for hypersonic boundary layers over an elliptic cone, performed by Quintanilha *et al.* (2022), reported strong transient growth of the non-modal perturbations in the vicinity of the cone tip and in the azimuthal locations away from both the centreline and the attachment line. It needs to be noted that the optimal perturbations calculated in these papers do not have a clear connection with the FSVDs, which is the central issue in the bypass transition.

In reality, there may be more complex factors to affect the boundary-layer transition at the surface of cruising hypersonic flying vehicles. The surface vibration, induced by either the mechanical vibration or the aeroelasticity, is a typical factor, but its mechanism affecting the transition onset is not well understood. Usually, the vibration frequency is rather low compared to the normal instability modes in hypersonic boundary layers, and their interaction could be too weak to cause an appreciable impact on natural transition. However, the vibration could affect the non-modal streaks because their frequency bands could be close to each other, leading to potential influences on the bypass transition. For an incompressible boundary layer, Ricco (2011) studied numerically the effect of steady spanwise wall forcing with a streamwise distribution on the linear evolution of streaks excited by FSVDs, and it was found that the streaks could be attenuated if the forcing has a streamwise length scale comparable with the FSVD-induced streaks and a spanwise length scale comparable to the boundary-layer thickness. Subsequently, Hicks & Ricco (2015) considered the effect of a spanwise oscillating wall on the streak development. In their formulation, the wavelengths of the streaks excited by low-frequency FSVDs are very long, which is taken to be comparable with the Reynolds number based on the boundary-layer thickness R_δ . Thus even if the amplitude of the spanwise velocity induced by the wall oscillation is as small as $O(R_\delta^{-1})$, the evolution of the streaks would be influenced by the oscillation. In this case, the spanwise generalised Stokes layer, together with the Blasius flow, was considered as the base flow for analysis of the streak evolution. It was found that the wall oscillation with this magnitude can enhance or suppress the streak energy remarkably, depending on the oscillation amplitude and frequency, as well as the FSVD property. Similar observations were made by Hack & Zaki (2014, 2015) using DNS, although their inflow conditions, the continuous modes of the Orr–Sommerfeld and Squire equations, were not appropriate (Wu & Dong 2016). The spanwise oscillating wall was also considered as a control strategy for the delay of bypass transition, as shown numerically in Negi *et al.* (2019). Additionally, the wall oscillation may also be employed as a drag reduction strategy in turbulent boundary layers (Jung, Mangiavacchi & Akhavan 1992; Toubert & Leschziner 2012; Ricco, Skote & Leschziner 2021).

However, the aforementioned works on the wall vibration effect were all focusing on low-speed boundary layers. For hypersonic boundary layers, the scenarios may be quite different. First, because the velocity of the oncoming stream is very high, the dimensionless vibrating amplitude should be much lower than that for low-speed boundary layers. Second, the frequency of the hypersonic boundary-layer instability is usually several hundred kilohertz, which is usually much higher than the vibration frequency

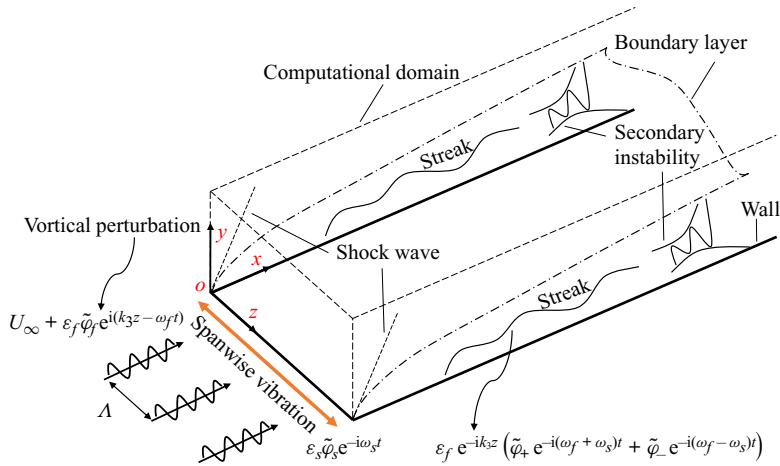


Figure 1. Sketch of the physical model, where the perturbations are defined in (2.3).

of the wall. Third, the entrainment of the FSVDs to hypersonic boundary layers and the subsequent excitation of non-modal streaks may be severely affected by the compressible effect (the temperature perturbation for a non-modal mode also shows a streaky feature, but with an even stronger amplitude, which was found to be an important feature by Ricco & Wu (2007) and Marensi *et al.* (2017)), as well as the interaction between the non-modal streaks and the wall vibration. Therefore, in this paper, we consider the effect of spanwise wall vibration on the evolution of the non-modal streaks subject to FSVDs in hypersonic boundary layers.

The rest of the paper is organised as follows. In §2, we introduce the physical model and mathematical details for calculating the response of a vibrating boundary layer to low-frequency FSVDs and nonlinear evolution of the excited boundary-layer streaky perturbations. The numerical approach for analysing the growth and the amplitude accumulation of the SI modes of the streaky profiles is introduced in §2.6. The numerical results of the linear evolution of the non-modal streaks are shown in §3, and the nonlinear development of the streaks and their SI analysis are shown in §4. Concluding remarks are provided in §5.

2. Physical model and mathematical descriptions

2.1. Physical model

In this paper, we study a hypersonic boundary-layer flow over a flat plate that is vibrating laterally, as sketched in figure 1. The plate is assumed to be infinitely thin, such that a rather weak oblique attached shock wave is formed from its leading edge. We introduce low-frequency FSVDs in the oncoming stream, which enter the boundary layer from the leading edge and generate streaks in the downstream locations. The streaks may undergo transient growths, and reach finite amplitudes if the FSVDs are relatively strong. Then the SI is likely to be excited, leading to bypass transition to turbulence eventually. Meanwhile, the vibrating wall induces another group of low-frequency perturbations to the flow field, which may interact with the FSVD-induced streaks, affecting their SI and leading to premature downstream transition or its delay.

The flow field is described by the three-dimensional (3-D) Cartesian coordinate (x^*, y^*, z^*) , with its origin located at the leading edge of the plate, where x^* , y^* and

z^* denote the streamwise, wall-normal and spanwise directions, respectively. The typical spanwise wavelength of the FSVDs, Λ , is taken to be the reference length, which is also roughly the length scale of the downstream boundary-layer thickness. The dimensionless coordinate system is $(x, y, z) = (x^*, y^*, z^*)/\Lambda$. The velocity field $\mathbf{u} = (u, v, w)$, density ρ , temperature T , pressure p , dynamic viscosity μ and time t are normalised by U_∞ , ρ_∞ , T_∞ , $\rho_\infty U_\infty^2$, μ_∞ and Λ/U_∞ , respectively. The flow is governed by two dimensionless parameters, the Reynolds number and the Mach number, which are defined as

$$R = \rho_\infty U_\infty \Lambda / \mu_\infty, \quad M = U_\infty / a_\infty, \quad (2.1a,b)$$

where a_∞ denotes the acoustic speed in the freestream.

2.2. Governing equations

The governing equations for a perfect-gas flow are the 3-D Navier–Stokes (N–S) equations, which can be found in Dong & Zhao (2021). The Sutherland viscosity law is employed, and we choose the ratio of the specific heats $\gamma = 1.4$ and the Prandtl number $Pr = 0.72$.

The instantaneous flow field $\boldsymbol{\varphi} \equiv (u, v, w, \rho, T, p)$ is decomposed as a two-dimensional (2-D) steady base flow $\boldsymbol{\Phi}_B \equiv (U_B, V_B, 0, \rho_B, T_B, P_B)$ and an unsteady perturbation $\check{\boldsymbol{\varphi}} \equiv (\check{u}, \check{v}, \check{w}, \check{\rho}, \check{T}, \check{p})$:

$$\boldsymbol{\varphi}(x, y, z, t) = \boldsymbol{\Phi}_B(x, y) + \check{\boldsymbol{\varphi}}(x, y, z, t). \quad (2.2)$$

In principle, the evolution of the perturbation $\check{\boldsymbol{\varphi}}$ can be calculated by DNS; however, this is too expensive, and most of the computational load is spent on the unnecessary high-order harmonics. Therefore, in this paper, we develop a more efficient means, namely, the harmonic weakly nonlinear Navier–Stokes (HWNNS) approach plus the nonlinear parabolised stability equation (NPSE) approach, which will be introduced in detail in §§ 2.4 and 2.5.

The excited perturbations $\check{\boldsymbol{\varphi}}$ include the boundary-layer response to an FSVD $\check{\boldsymbol{\varphi}}_f$ (with frequency ω_f), a vibration-induced perturbation $\check{\boldsymbol{\varphi}}_s$ (with frequency ω_s), the excited perturbation due to their mutual interaction, $\check{\boldsymbol{\varphi}}_+$ (with frequency $\omega_f + \omega_s$) and $\check{\boldsymbol{\varphi}}_-$ (with frequency $\omega_f - \omega_s$), and their high-order harmonics. As confirmed by DNS, the amplitudes of the high-order harmonics are lower than those of the direct-interaction-driven perturbations $\check{\boldsymbol{\varphi}}_\pm$. Therefore, the former are truncated in the HWNNS analysis. We consider the frequencies of the FSVD and wall vibration to be low, i.e. $\omega_f \ll 1$ and $\omega_s \ll 1$; then the boundary-layer perturbations $\check{\boldsymbol{\varphi}}$ have long length scales in the streamwise direction, $\lambda_x \gg 1$. Thus $\partial_x \sim \lambda_x^{-1} \ll 1$. Note that even when the frequency is zero, the streamwise length scale is still finite due to the presence of the non-parallelism of the base flow, which is $O(R)$. Because the wall is vibrating laterally as a whole, there is no specific length scale for $\check{\boldsymbol{\varphi}}_s$ in the z -direction, thus $\check{\boldsymbol{\varphi}}_s$ is independent of z . Additionally, from a preliminary analysis, it is found that the vibration-induced perturbation only has a non-zero \check{w}_s component, namely, $\check{\boldsymbol{\varphi}}_s = (0, 0, \check{w}_s(x, y), 0, 0, 0)$. The spanwise length scales of $\check{\boldsymbol{\varphi}}_f$ and $\check{\boldsymbol{\varphi}}_\pm$ are determined by the spanwise wavelength of the FSVD, which is taken to be $O(1)$ from the normalisation in § 2.1; then we have $\partial_z(\check{\boldsymbol{\varphi}}_{f,\pm}) \sim \check{\boldsymbol{\varphi}}_{f,\pm}$.

Since the base-flow velocity is $U_B = O(1)$, the streamwise convection of the boundary-layer perturbations scales like $U_B \partial_x \check{u}_{f,\pm} \sim \lambda_x^{-1} \check{u}_{f,\pm}$, while the vibration-induced spanwise redistribution is $w_s \partial_z \check{u}_{f,\pm} \sim w_s \check{u}_{f,\pm}$, where $w_s = \check{w}_s \exp(-i\omega_s t) + \check{w}_s^C \exp(i\omega_s t)$ denotes the spanwise velocity induced by the wall vibration. In what follows, a superscript C denotes the complex conjugate. Following Ricco (2011) and Hicks & Ricco (2015), if we take $w_s \sim \lambda_x^{-1} \ll 1$, then the leading-order balance in the momentum equations

determines $U_B \partial_x \check{\varphi}_f \sim \check{w}_s \partial_z \check{u}_- + \check{w}_s^C \partial_z \check{u}_+$, $U_B \partial_x \check{\varphi}_+ \sim \check{w}_s \partial_z \check{u}_f$ and $U_B \partial_x \check{\varphi}_- \sim \check{w}_s^C \partial_z \check{u}_f$. Thus the perturbations $\check{\varphi}_f$ and $\check{\varphi}_\pm$ are coupled. Additionally, the back action of the mutual interaction of $\check{\varphi}_f$ and $\check{\varphi}_\pm$ on \check{w}_s is rather small; an estimate can be obtained by analysing the spanwise momentum equation of $\check{\varphi}_s$ as follows. The convection term in the z momentum equation scales as $U_B \partial_x \check{w}_s \sim \lambda_x^{-1} \check{w}_s$, while the mutual interaction of $\check{\varphi}_f$ and $\check{\varphi}_\pm$ scales as $\check{u}_f \partial_x \check{w}_- \sim \lambda_x^{-2} \check{u}_f \check{u}_-$, where the condition $\check{w}_- \sim \lambda_x^{-1} \check{u}_-$ is imposed from the continuity equation. As mentioned before, we take $\check{w}_s \sim \lambda_x^{-1}$; then the mutual interaction of $\check{\varphi}_f$ and $\check{\varphi}_\pm$ is negligible. In such a situation, the vibration-induced perturbation, to leading order, is governed by the linearised N–S system without any inhomogeneous forcing. The high-order harmonics, including the perturbations excited by the self-interactions of $\check{\varphi}_f$, $\check{\varphi}_\pm$ and their mutual interactions, are $O(\check{\varphi}_f^2)$, much smaller than the magnitude of each individual. Because $\check{\varphi}_s$ only has non-zero \check{w}_s component with no spanwise length scale, its self-interaction does not induce further perturbations.

From the above analysis, we can express the perturbation field as

$$\begin{aligned} \check{\varphi} = \sum & \left[\mathcal{E}_s \tilde{\varphi}_s(x, y) \exp(-i\omega_s t) + \mathcal{E}_f \exp(ik_3 z) \left(\tilde{\varphi}_f(x, y) \exp(-i\omega_f t) \right. \right. \\ & \left. \left. + \tilde{\varphi}_+(x, y) \exp(-i(\omega_f + \omega_s)t) + \tilde{\varphi}_-(x, y) \exp(-i(\omega_f - \omega_s)t) \right) + \dots \right] \\ & + \text{c.c.} + \text{h.o.h.}, \end{aligned} \tag{2.3}$$

where $\mathcal{E}_{s,f} \ll 1$ denotes the amplitude of each individual perturbation, $\omega \in \mathbb{R}$ is the dimensionless frequency, $k_3 \in \mathbb{R}$ is the dimensionless spanwise wavenumber of the FSVD, $\tilde{\varphi} \in \mathbb{C}$ is the perturbation profile, and c.c. is the complex conjugate. Note that for simplicity, we consider only one spanwise wavenumber k_3 in the HWNNS calculations. However, in the subsequent NPSE calculations, perturbations with both positive and negative spanwise wavenumbers $\pm k_3$ are considered, as will be demonstrated in (4.1), which is consistent with the set-up of Ricco *et al.* (2011) and Marensi *et al.* (2017). In the vicinity of the leading edge, because the base flow shows strong non-parallelism and the amplitudes of the high-order harmonics (h.o.h.) are negligibly small, we employ the harmonic linearised Navier–Stokes (HLNS) approach (Zhao, Dong & Yang 2019) to calculate $\tilde{\varphi}_s$, and the HWNNS approach to calculate $\tilde{\varphi}_f$ and $\tilde{\varphi}_\pm$ (to be introduced in § 2.4.2); in the downstream region, where the base flow has reached the self-similarity state but the higher-order harmonics have reached the finite-amplitude state, the NPSE approach (Zhao *et al.* 2016) is employed to calculate the mutual interaction of the Fourier modes.

2.3. Numerical approaches for the base-flow calculation

The 2-D base flow $\Phi_B(x, y)$ is governed by the steady N–S equations. In the numerical process, we select a rectangular box ($x \in [x_0, x_I]$, $y \in [0, y_J]$, with $x_0 = -0.426$, $x_I = 300$ and $y_J = 90$) as the computational domain, shown in figure 2, and discretise it into $(I + 1) \times (J + 1)$ grid points. Here, the inlet of the computational domain x_0 is chosen to be slightly upstream of the plate leading edge for numerical convenience, and it has been confirmed that changing x_0 to another negative value does not change the numerical results. Each grid point is labelled by (x_i, y_j) , with $i \in [0, I]$ and $j \in [0, J]$ in the streamwise and wall-normal directions, respectively. Using the Lax–Friedrichs flux splitting method, the convective terms are discretised by the fifth-order weighted essentially non-oscillatory (WENO) scheme (Jiang & Shu 1996); the viscous terms are

Influence of wall vibration on non-modal perturbations

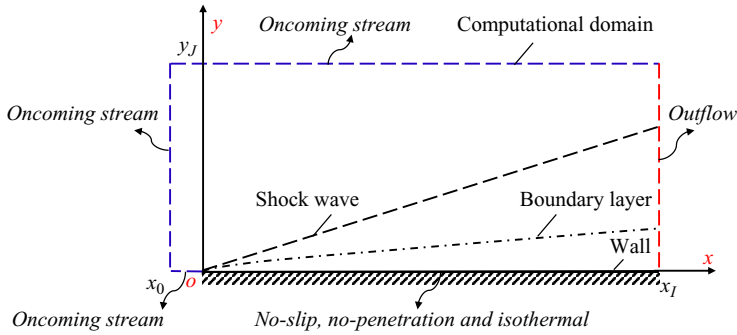


Figure 2. Sketch of the computational domain and the boundary conditions of the base-flow calculation (not to scale).

discretised by the fourth-order central finite difference scheme; the lower–upper symmetric Gauss–Seidel (LU–SGS) method is used for time advancing. The boundary conditions are set as follows. The no-slip, no-penetration and isothermal conditions $(U_B, V_B, W_B, T_B) = (0, 0, 0, T_w)$ are imposed at the wall ($x \in [0, x_I]$ and $y = 0$), where T_w denotes the dimensionless wall temperature. The inflow condition ($x = x_0, y \in [0, y_J]$), the centreline condition ($x \in (x_0, 0), y = 0$) and the upper boundary condition ($x \in (x_0, x_I], y = y_J$) are set to be the oncoming stream; the extrapolated boundary condition is employed at the outlet ($x = x_I, y \in (0, y_J)$).

2.4. The HLNS and HWNNS approaches describing the perturbation evolution

2.4.1. The HLNS approach for calculating the boundary-layer response to lateral vibrations

As illustrated in § 2.2, the vibration-induced perturbation is governed by the linearised N–S equation system, which therefore can be solved by the HLNS approach. The excited perturbation field $\tilde{\varphi}_s(x, y) \exp(-i\omega_s t)$, which is independent of z , satisfies the linear system

$$\mathcal{L}(\omega_s) \tilde{\varphi}_s(x, y) \equiv \left(\tilde{\mathbf{D}} + \tilde{\mathbf{A}} \partial_x + \tilde{\mathbf{B}} \partial_y + \mathbf{V}_{xx} \partial_{xx} + \mathbf{V}_{yy} \partial_{yy} + \mathbf{V}_{xy} \partial_{xy} \right) \tilde{\varphi}_s(x, y) = 0, \quad (2.4)$$

where \mathcal{L} represents the linearised N–S operator. The coefficient matrices $\tilde{\mathbf{D}}, \tilde{\mathbf{A}}, \tilde{\mathbf{B}}, \mathbf{V}_{xx}, \mathbf{V}_{yy}$ and \mathbf{V}_{xy} can be found in the appendix of Zhao *et al.* (2019). Such an approach that allows the time-domain problems to be solved quickly by converting them into Fourier series has also been applied in some previous works (Gopinath & Jameson 2005, 2006). The perturbations at all boundaries are set to be zero except at the wall, where $\tilde{w}_s = 1$ is imposed. We introduce the unknown vector $\tilde{\mathbf{q}} \equiv (\tilde{\varphi}_{f,0,0}, \tilde{\varphi}_{f,0,1}, \dots, \tilde{\varphi}_{f,0,J}, \dots, \tilde{\varphi}_{f,I,0}, \dots, \tilde{\varphi}_{f,I,J})$, where $\tilde{\varphi}_{f,i,j}$ denotes the value of $\tilde{\varphi}_f$ at (x_i, y_j) . Then $\tilde{\mathbf{q}}$ is governed by a system of linear algebraic equations,

$$\mathbf{M} \tilde{\mathbf{q}} = \tilde{\mathbf{r}}, \quad (2.5)$$

where the coefficient matrix \mathbf{M} can be readily derived from (2.4), and $\tilde{\mathbf{r}}$ denotes the inhomogeneous forcing from the wall. Here, the streamwise non-parallelism is retained, such that the rapid distortion of the perturbation around the leading edge can be calculated. The computational domain for the HLNS calculation is the same as that for the base-flow calculation; see domain (I) in figure 3. It needs to be noted that our numerical scheme

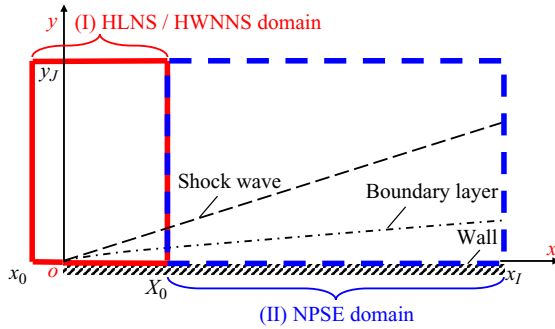


Figure 3. Sketch of the computational domains for the HLNS/HWNNS and NPSE calculations.

for HLNS and the following HWNNS is not adequate to deal with the perturbations around a shock wave. However, in the present flat-plate model, the leading-edge oblique shock wave is rather weak, and its impact on the oncoming perturbations is quite limited. Therefore, our scheme works well on describing the perturbation evolution, as confirmed by comparing with the DNS results in [Appendix B](#).

It is worth noting that the selection of the primitive variables $\tilde{\varphi}$ as the unknowns in (2.4) and the following equation system (2.6) is not unique, and an alternative option is to choose the conserved variables. The latter approach is particularly advantageous when dealing with strong shock waves in the flow field. However, in the present problem, as the oblique shock wave forming from the leading edge is relatively weak, both approaches would yield identical results.

2.4.2. The HWNNS approach for calculation of the excited perturbations $\tilde{\varphi}_f$ and $\tilde{\varphi}_{\pm}$

According to the scaling estimate in § 2.2, the excited perturbations $\tilde{\varphi}_f$ and $\tilde{\varphi}_{\pm}$ are governed by the inhomogeneous equations

$$\mathcal{L}(\omega_f) \tilde{\varphi}_f(x, y) = \mathcal{E}_s \left(\mathbf{b}(\tilde{\varphi}_s^C, -\omega_s) \tilde{\varphi}_+ + \mathbf{b}(\tilde{\varphi}_s, \omega_s) \tilde{\varphi}_- \right), \quad (2.6a)$$

$$\mathcal{L}(\omega_f + \omega_s) \tilde{\varphi}_+(x, y) = \mathcal{E}_s \mathbf{b}(\tilde{\varphi}_s, \omega_s) \tilde{\varphi}_f, \quad \mathcal{L}(\omega_f - \omega_s) \tilde{\varphi}_-(x, y) = \mathcal{E}_s \mathbf{b}(\tilde{\varphi}_s^C, -\omega_s) \tilde{\varphi}_f, \quad (2.6b,c)$$

where \mathbf{b} is a coefficient matrix appearing as inhomogeneous forcing of the linearised N–S operator. The generic form of $\mathbf{b}(\tilde{\varphi}_1, \omega) \tilde{\varphi}_2 = [b^{(1)}, b^{(2)}, b^{(3)}, b^{(4)}, b^{(5)}]^T$ is expressed as

$$\left. \begin{aligned} b^{(1)} &= -ik_3 \tilde{w}_1 \tilde{\rho}_2, & b^{(2)} &= -ik_3 \rho_B \tilde{w}_1 \tilde{u}_2, & b^{(3)} &= -ik_3 \rho_B \tilde{w}_1 \tilde{v}_2, \\ b^{(4)} &= -\rho_B (\tilde{w}_{1,x} \tilde{u}_2 + \tilde{w}_{1,y} \tilde{v}_2 + ik_3 \tilde{w}_1 \tilde{w}_2) - (U_B \tilde{w}_{1,x} + V_B \tilde{w}_{1,y} - i\omega \tilde{w}_1) \tilde{\rho}_2, \\ b^{(5)} &= \frac{-ik_3 \tilde{w}_1}{\gamma} \left[\rho_B \tilde{T}_2 + (1 - \gamma) T_B \tilde{\rho}_2 \right]. \end{aligned} \right\} \quad (2.7)$$

It is easy to see that in the incompressible limit, if the high-order interactions are truncated, then (2.6) is equivalent to (2.14) of Hicks & Ricco (2015). The only difference is that in our system, the vibration-induced spanwise redistribution term \mathbf{b} appears as an inhomogeneous forcing term on the right-hand side of each equation, while in Hicks & Ricco (2015), the Stokes layer induced by the lateral vibration is considered as a part of the base flow. The high-order interactions will be considered by the NPSE in § 2.5. Since $\tilde{\varphi}_s$ is obtained

beforehand, the system (2.6) is indeed a coupled linear system, but in the numerical process (as will be shown at the end of this subsection) we treat these terms as the first-order nonlinear forcing in each iterative step. The advantage of this treatment is that the linear operator \mathcal{L} on the left-hand side of each subequation of (2.6) is the same as that in (2.4), rendering an easy extension of the HLNS framework. Because only the first-order nonlinear terms are included here, this approach is named the harmonic weakly nonlinear Navier–Stokes (HWNNS) approach. At first glance, the small quantity \mathcal{E}_s appearing on the right-hand side of each equation in (2.6) is a little unsatisfactory. However, we would like to emphasise that the linear operator \mathcal{L} is also small due to the low-frequency and long-wavelength nature (i.e. $\sim \lambda_x^{-1}$), and the magnitudes of \mathcal{E}_s and \mathcal{L} are taken to be comparable in this paper.

For a still-wall case where $\mathcal{E}_s = 0$, the perturbations $\tilde{\varphi}_\pm$ are both zero, and (2.6a) is reduced to a homogeneous equation system, with the inhomogeneous forcing appearing only at the oncoming stream. An FSVD with frequency ω_f and the streamwise, wall-normal and spanwise wavenumbers (k_1, k_2, k_3) is expressed as

$$\hat{\varphi}_f \exp(i(k_1x + k_2y + k_3z - \omega_f t)) + \text{c.c.}, \quad (2.8)$$

where $\hat{\varphi}_f \equiv (\hat{u}_f, \hat{v}_f, \hat{w}_f, 0, 0, 0)$. Substituting (2.8) into the linearised N–S equations, we obtain the dispersion relation of the FSVD, $k_1 = \omega_f + O(R^{-1/2})$ (Wu & Dong 2016). Note that we are interested in the entrainment of the low-frequency perturbations, so $k_1 \ll k_2 \sim k_3 \sim 1$. Without loss of generality, we take the spanwise vorticity to be zero, i.e. $k_1 \hat{v}_f - k_2 \hat{u}_f = 0$. Note that this is an arbitrary choice, but the excitation process of the boundary-layer perturbation for this condition is representative, as long as the magnitudes of the wavenumbers in the three directions are fixed. Combining with the continuity equation ($k_1 \hat{u}_f + k_2 \hat{v}_f + k_3 \hat{w}_f = 0$), and taking the unit perturbation kinetic energy as the normalisation condition ($(\hat{u}_f^2 + \hat{v}_f^2 + \hat{w}_f^2)/2 = 1$), we obtain

$$(\hat{u}_f, \hat{v}_f, \hat{w}_f) = \sqrt{\frac{2}{(k_1^2 + k_2^2)(k_1^2 + k_2^2 + k_3^2)}} \left(-k_1 k_3, -k_2 k_3, k_1^2 + k_2^2 \right). \quad (2.9)$$

For (2.6a), the boundary conditions at $(x = x_0, y \in [0, y_J])$, $(x \in (x_0, x_I), y = y_J)$ and $(x \in (x_0, 0), y = 0)$ are the FSVD $\tilde{\varphi}_f = \hat{\varphi}_f \exp(i(k_1x + k_2y))$, appearing as an inhomogeneous forcing to the linear system; the extrapolated boundary condition is employed at the outlet $x = x_I$; the zero-perturbation conditions are imposed at the other boundaries.

Thus for a still wall, the excited perturbation $\tilde{\varphi}_f$ is obtained by directly solving the HLNS equation system $\mathcal{L}(\omega_f) \tilde{\varphi}_f(x, y) = 0$, whereas for a spanwise vibrating wall, an iterative scheme is employed to deal with the coupled system (2.6).

- (i) Set $\tilde{\varphi}_\pm = 0$ at the beginning.
- (ii) Solve for $\tilde{\varphi}_f$ from (2.6a) subject to the freestream forcing.
- (iii) Calculate the inhomogeneous forcing of (2.6b,c) from the obtained $\tilde{\varphi}_f$, and solve for $\tilde{\varphi}_\pm$.
- (iv) Calculate the inhomogeneous forcing of (2.6a), and go to step (ii) until the solution converges.

In steps (ii) (except for the first round of the iteration) and (iii), each governing equation has a harmonic linear operator on its left-hand side, and only the first-order nonlinear interaction terms are retained on its right-hand side, which is the reason for the name of the HWNNS approach.

2.5. The NPSE for the nonlinear evolution of the boundary-layer perturbations

In the HWNNs calculations illustrated in § 2.4, the high-order harmonics are truncated, which may be important in the downstream regions. Therefore, the NPSE approach (Chang & Malik 1994; Zhao *et al.* 2016) is employed in the downstream region; see domain (II) in figure 3. Such a treatment is acceptable for the following reasons: (1) in the vicinity of the leading edge, the perturbation deforms rapidly, but with a small amplitude, for which the HLNS/HWNNs approach is rather efficient; (2) in the downstream region, i.e. $x \geq X_0$, the perturbation evolves slowly in the x -direction, but with a sufficiently high amplitude for nonlinearity, for which the NPSE approach works well. Note that in § 2.4, the HLNS/HWNNs calculations were performed from x_0 to x_l , but the flow field in $x \in (X_0, x_l)$ is not needed physically. However, for code verification, we can compare this flow field with the NPSE and DNS calculations for a small \mathcal{E}_f , say $\mathcal{E}_f = 10^{-8}$, as will be shown in figures 14 and 30.

In Ricco *et al.* (2011), Marensi *et al.* (2017), Xu *et al.* (2017) and Xu, Liu & Wu (2020), the entrainment of FSVDs and the excitation of the boundary-layer streaks were formulated by the nonlinear boundary-region equation, which is able to deal with both the rapid distortion in the leading-edge vicinity and the nonlinearity in the downstream region. For the present physical model, our numerical approach, combining HLNS/HWNNs with the NPSE, in principle reproduces the nonlinear boundary-region calculations. However, our approach is easy to apply to more complex situations, such as a hypersonic boundary layer over a blunt body, for which the impacts of the bow-shaped shock wave and the entropy layer need to be considered. The present work can be regarded as the first step to solve more complex problems.

In the NPSE, the perturbation $\check{\varphi}(x, y, z, t)$ in (2.3) is expressed in terms of a truncated Fourier series,

$$\check{\varphi}(x, y, z, t) = \sum_{m=-\mathcal{M}}^{\mathcal{M}} \sum_{n=-\mathcal{N}}^{\mathcal{N}} \mathcal{E}_{m,n} \check{\varphi}_{m,n}(x, y) \exp \left(i \left[\int_{X_0}^x \alpha_{m,n}(\bar{x}) d\bar{x} + n\beta_0 z - m\omega_0 t \right] \right), \tag{2.10}$$

where $\omega_0 \in \mathbb{R}$ and $\beta_0 \in \mathbb{R}$ are the fundamental frequency and spanwise wavenumber, respectively, m and n denote the orders of ω and β , respectively, $\mathcal{E}_{m,n} \ll 1$ and $\alpha_{m,n} \in \mathbb{C}$ represent the amplitude and complex wavenumber of the harmonic mode, respectively, $\check{\varphi}_{m,n} \equiv (\tilde{u}_{m,n}, \tilde{v}_{m,n}, \tilde{w}_{m,n}, \tilde{\rho}_{m,n}, \tilde{T}_{m,n}, \tilde{p}_{m,n})$ is the complex shape function that varies slowly with x , $X_0 = 60$ represents the inlet of the NPSE domain, and \mathcal{M} and \mathcal{N} denote the limiting orders of the truncation for the frequency and spanwise wavenumber, respectively. Here, ω_0 is the common divisor of ω_f and ω_s , if both frequencies are non-zero. Otherwise, ω_0 should be selected as the non-zero value of ω_f and ω_s . The value β_0 is chosen to be k_3 .

Substituting (2.10) into the compressible N–S equations, subtracting out the base-flow terms, and neglecting the terms associated with $\partial_{xx}\check{\varphi}_{m,n}$ and $\partial_{xy}\check{\varphi}_{m,n}$, we obtain the NPSEs

$$\left(\tilde{A}_{m,n} \partial_x + \tilde{B}_{m,n} \partial_y + \tilde{D}_{m,n} + V_{yy} \partial_{yy} \right) \check{\varphi}_{m,n}(x, y) = \tilde{F}_{m,n} \exp \left(-i \int_{X_0}^x \alpha_{m,n}(\bar{x}) d\bar{x} \right), \tag{2.11}$$

where the coefficient matrices $\tilde{A}_{m,n}$, $\tilde{B}_{m,n}$, $\tilde{D}_{m,n}$, V_{yy} and the nonlinear term $\tilde{F}_{m,n}$ can be found in Zhao *et al.* (2016). Since the ∂_{xx} terms are neglected, the elliptic N–S equations are parabolised, such that a marching scheme can be employed in the numerical process. The NPSE calculation begins at a position $x = X_0$, as depicted in figure 3. This position is

chosen to be downstream of the rapid distortion region at the leading edge, and upstream of the region where higher-order harmonics become significant. The inflow perturbation profiles and their amplitudes are obtained through the HLNS calculations. Denote the Fourier components of the FSVD $\tilde{\varphi}_f$ and vibration $\tilde{\varphi}_s$ by $(m_1, 1)$ and $(m_2, 0)$, respectively. The perturbations $\tilde{u}_{m,n}$, $\tilde{v}_{m,n}$, $\tilde{w}_{m,n}$ and $\tilde{T}_{m,n}$ are all set to be zero at the wall, except $\tilde{w}_{m_2,0} = 1$. At the upper boundary, we set $(\tilde{u}_{m_1,1}, \tilde{v}_{m_1,1}, \tilde{w}_{m_1,1}) = \hat{\varphi}_f \exp(i(k_1x + k_2y))$ and $\partial_y \tilde{v}_{0,0} = 0$, and the other quantities are all set to be zero. If $\tilde{F}_{m,n}$ is set to be zero, then the system (2.11) is reduced to the linear parabolised stability equation (LPSE), which can be used to trace the linear amplification of each Fourier component. The NPSE code has been applied in a few previous works (Zhao *et al.* 2016; Song, Zhao & Dong 2023a), which were confirmed to be sufficiently accurate in comparison with DNS.

2.6. The SI analysis of streaks

The streaks themselves do not lead to transition; however, they could support rapid growths of high-frequency perturbations via the SI regime. Since the length scale of the SI modes is much shorter than that of the streaky base flow, we can introduce the parallel-flow assumption for the SI analysis. The streaky base flow is expressed as $\check{\Phi}_B(y, z; \check{x}, \check{t}) \equiv [\check{U}_B, 0, 0, \check{\rho}_B, \check{T}_B, \check{P}_B]$, which is a superposition of the 2-D base flow and the NPSE solutions at a streamwise position \check{x} and a time instant \check{t} :

$$\begin{aligned} \check{\Phi}_B(y, z; \check{x}, \check{t}) &= \Phi_B(y; \check{x}) \\ &+ \sum_{m=-\mathcal{M}}^{\mathcal{M}} \sum_{n=-\mathcal{N}}^{\mathcal{N}} \mathcal{E}_{m,n} \tilde{\varphi}_{m,n}(y; \check{x}) \\ &\times \exp(i(nk_3z - m\omega_0\check{t})) \exp\left(i \int_{X_0}^{\check{x}} \alpha_{m,n}(\bar{x}) d\bar{x}\right), \end{aligned} \quad (2.12)$$

where \mathcal{M} , \mathcal{N} , \mathcal{E} , $\tilde{\varphi}$ and ω_0 were defined in (2.10).

For simplicity, we perform the temporal-mode SI analysis, and the perturbations $\check{\Psi}_{SI}(x, y, z, t) \equiv (\check{u}_{SI}, \check{v}_{SI}, \check{w}_{SI}, \check{\rho}_{SI}, \check{T}_{SI}, \check{p}_{SI})$ are expressed as

$$\left. \begin{aligned} \check{\Psi}_{SI}(x, y, z, t) &= \mathcal{E}_{SI} \tilde{\varphi}_{SI}(y, z) \exp(i(\alpha x - \omega t)) \exp(i\sigma_d k_3 z) + \text{c.c.}, \\ \tilde{\varphi}_{SI}(y, z) &= \sum_{n=-\mathcal{N}_{SI}}^{\mathcal{N}_{SI}} \hat{\varphi}_{SI,n}(y) \exp(ink_3 z), \end{aligned} \right\} \quad (2.13)$$

where $\alpha \in \mathbb{R}$ and $\omega = \omega_r + i\omega_i \in \mathbb{C}$ are the streamwise wavenumber and complex frequency of the SI mode, respectively, with ω_i denoting its temporal growth rate. Here, \mathcal{E}_{SI} is the amplitude, and \mathcal{N}_{SI} is the truncation order of the Fourier series. In this paper, we set $\mathcal{N}_{SI} = 8$. Also, $\sigma_d \in [0, 0.5]$ is a detuning parameter, which is zero for a fundamental mode, 0.5 for a subharmonic mode and another value for the detuned mode, and all of them could be unstable with comparable growth rates; see Ren & Fu (2015). As a representative study, we focus only on the fundamental mode in this paper. Substituting (2.12) and (2.13) into the linearised N–S equations, we arrive at a linear equation system,

$$\left(\tilde{D}_{SI} + \tilde{B}_{SI} \partial_y + \tilde{C}_{SI} \partial_z + V_{yy} \partial_{yy} + V_{zz} \partial_{zz} + V_{yz} \partial_{yz}\right) \tilde{\varphi}_{SI}(y, z) = 0. \quad (2.14)$$

M	R	T_∞	T_w	T_w/T_{ad}	Description
5.92	33 000	48.59 K	3.48	0.50	Cold wall

Table 1. Parameters for case studies.

The coefficient matrices \tilde{D}_{SI} , \tilde{B}_{SI} and \tilde{C}_{SI} are given by

$$\tilde{D}_{SI} = D - (i\omega)\Gamma + (i\alpha)A + (i\alpha)^2 V_{xx}, \tag{2.15a}$$

$$\tilde{B}_{SI} = B + (i\alpha)V_{xy}, \tag{2.15b}$$

$$\tilde{C}_{SI} = C + (i\alpha)V_{xz}, \tag{2.15c}$$

where the coefficient matrices D , Γ , A , B , C , V_{yy} , V_{zz} , V_{yz} , V_{xx} , V_{xy} and V_{xz} depend on $\check{\Phi}_B$ and can be found in the appendix of Zhao *et al.* (2019). The system (2.14) with the homogeneous boundary conditions forms a generalised eigenvalue system,

$$\mathcal{A}\tilde{\varphi}_{SI}(y, z) = \omega\mathcal{B}\tilde{\varphi}_{SI}(y, z), \tag{2.16}$$

with ω being the eigenvalue, and the coefficient matrices \mathcal{A} and \mathcal{B} are readily derived from (2.14). The Arnoldi iterative method is employed to search the eigenvalues initially, and the Rayleigh quotient iteration method is used to confirm its accuracy, as has been used in Han *et al.* (2021) and Song, Dong & Zhao (2023*b*).

3. Numerical results of the base flow and the linear evolution of the perturbations

3.1. Base flow

The controlling parameters selected in this paper are listed in table 1. The base-flow calculation is based on the 2-D domain $x \in [-0.426, 300]$ and $y \in [0, 90]$. We employ 1201 grid points in the x -direction, with 515 grid points clustered near the leading edge ($x \leq 60$), and 301 grid points clustered near the wall are employed in the y -direction. Figure 4(a) shows the contours of the pressure P_B , where the yellow line forming from the leading edge with an oblique angle 9.54° , approximately equal to $\tan^{-1}(1/M)$, denotes the oblique attached shock wave. Figures 4(b) and 4(c) compare the U_B and T_B profiles with the compressible Blasius solutions at different streamwise positions. The agreement between the two families of curves confirms the accuracy of our base-flow calculations.

3.2. Instability property

Although we are not primarily focusing on the excitation and evolution of normal modes in this paper, they could exist in a downstream position, where the local Reynolds number is relatively large. For supersonic boundary layers with $M > 4$, there exist multiple unstable modes, and the second mode is usually more unstable (Mack 1987). In this paper, we are interested in the 3-D low-frequency perturbations, and the neutral curves of the 3-D Mack first modes for $\beta = 0.33, 1, 2$ and 2.67 in the $x-\omega$ plane are plotted in figure 5(a). For $\omega < 0.2$ and $\beta \leq 1$, the frequency of the neutral first mode decreases with increase of x , indicating an enlargement of the unstable zone in the low-frequency band. For higher β values, the unstable zone shrinks, and no unstable first mode is observed for $\omega \leq 0.05$. In figure 5(b), the neutral curve in the $\omega-x$ plane for $\beta = 1$

Influence of wall vibration on non-modal perturbations

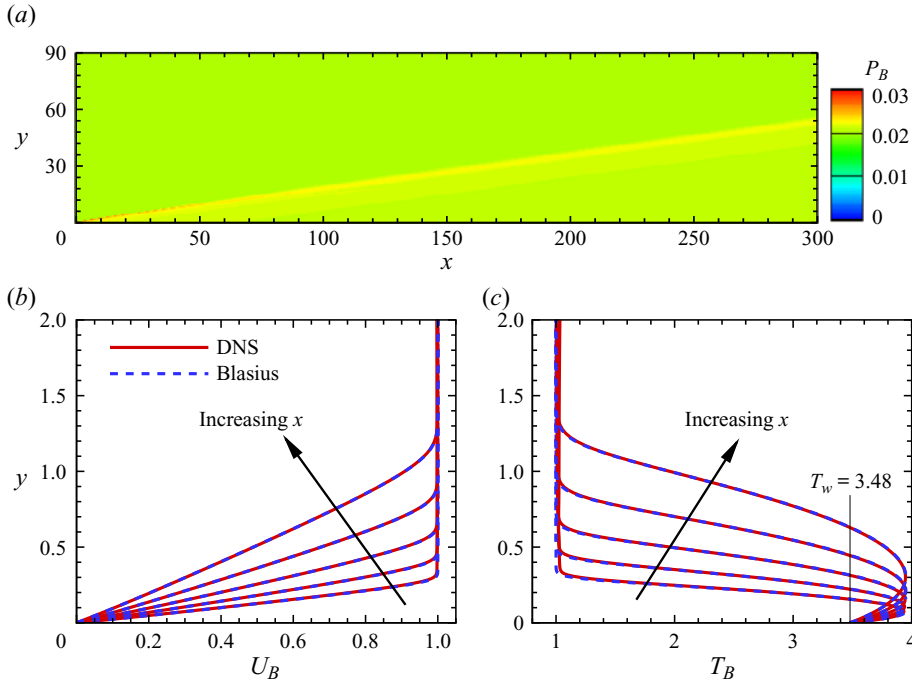


Figure 4. Base flow. (a) Contours of the mean pressure P_B . (b,c) Comparisons of the streamwise velocity U_B and temperature T_B profiles with the compressible Blasius solutions at $x = 15, 30, 60, 120$ and 240 .

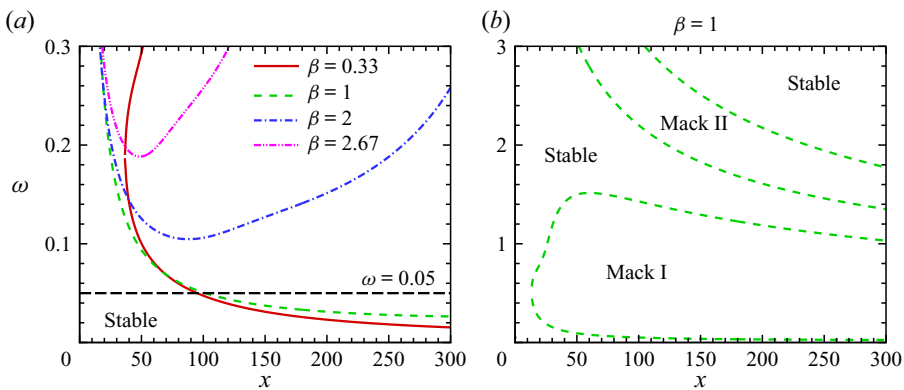


Figure 5. (a) Neutral curves of the 3-D Mack modes for $\beta = 0.33, 1, 2$ and 2.67 . (b) Neutral curves of the first and second modes in a wider frequency band for $\beta = 1$.

in a wider frequency band is plotted, and the Mack second mode and the first mode of the upper branch, appearing when $\omega = O(1)$, are excluded in the discussion of this paper.

3.3. Linear response of a still boundary layer to FSVDs

In this subsection, we consider the results for still walls. For the HLNS calculations, the same computational domain as in § 3.1 is used, but the number of grid points in the

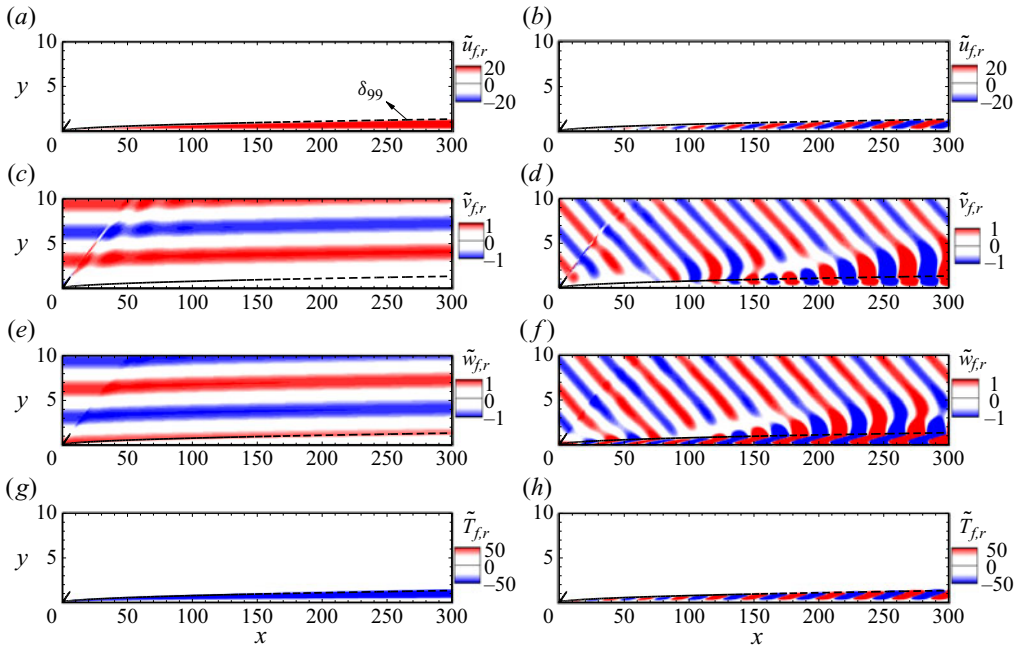


Figure 6. Contours of the real parts of \tilde{u}_f , \tilde{v}_f , \tilde{w}_f and \tilde{T}_f excited by the low-frequency FSVDs with $k_2 = k_3 = 1$, for (a,c,e,g) $\omega_f = 0$, (b,d,f,h) $\omega_f = 0.17$. The dashed lines mark the nominal boundary-layer thickness.

x -direction is reduced to 401. To characterise the ratio of k_2 to k_3 , we introduce an oblique wave angle $\Theta \equiv \tan^{-1}(k_2/k_3)$. Choosing $k_2 = k_3 = 1$ ($\Theta = 45^\circ$), we plot the contours of the perturbation field $\tilde{\varphi}_f$ in figure 6. For $\omega_f = 0$, the perturbations \tilde{v}_f and \tilde{w}_f show long streamwise length scales in the external stream, and a mild kink appears at the oblique shock wave. In the boundary layer, \tilde{v}_f and \tilde{w}_f are rather small, but the perturbations \tilde{u}_f and \tilde{T}_f undergo drastic amplifications, agreeing with Leib *et al.* (1999) and Ricco & Wu (2007). For an FSVD with $\omega_f = 0.17$, the overall behaviour of the perturbation field remains the same, but a finite streamwise length scale is observed due to the finite wavelength of the FSVD.

Figure 7(a) plots the streamwise evolution of the amplitude of the streamwise velocity perturbation $\tilde{U}_f(x) = \max_y(|\tilde{u}_f(x, y)|)$ for five representative frequencies ($\omega_f = 0, 0.05, 0.1, 0.17$ and 0.33). Each curve shows a drastic increase in the vicinity of the leading edge, i.e. $x < 15$, indicating a rapid adjustment of the perturbation in a region where the non-parallelism of the mean flow is strong; after a mild decay, it grows until the end of the calculation. Overall, the amplitude \tilde{U}_f increases as the frequency increases. The temperature perturbation $\tilde{T}_f = \max_y(|\tilde{T}_f(x, y)|)$ is one order of magnitude greater than that of \tilde{U}_f , agreeing with the solutions given by the boundary-region equations in Ricco & Wu (2007). In the downstream region, the non-stationary perturbations would enter the unstable zone of the Mack first mode, and a comparison with the predictions by linear stability theory (LST), shown by the open symbols, and LPSE, shown by the filled symbols, is provided. The disparity between the LST and LPSE calculations arises from the consideration of non-parallelism in the base flow, which is neglected in the former but retained in the latter. The overall agreement between the HLNS calculations and the LST/LPSE predictions is evident in the region approximately downstream of the neutral

Influence of wall vibration on non-modal perturbations

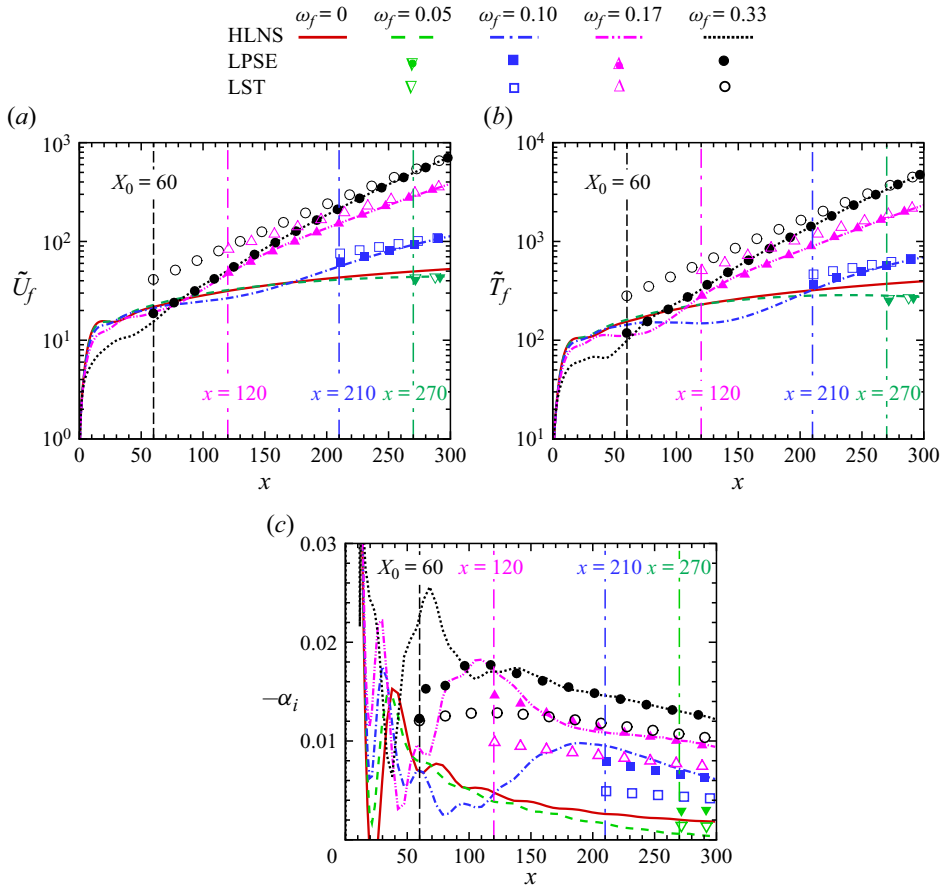


Figure 7. Evolution of (a) \tilde{U}_f , (b) \tilde{T}_f , and (c) the growth rate $-\alpha_i$, for $k_2 = k_3 = 1$. The vertical lines denote the intersection positions of the non-modal and modal perturbations.

points of the Mack first mode, shown by the vertical lines. A clearer observation of each curve is provided by plotting the streamwise evolution of the growth rates $(\tilde{U}_f^{-1} d\tilde{U}_f/dx)$ for HLNS and LPSE, and $-\alpha_i$ for LST in figure 7(c). Again, the HLNS calculations agree well with the LPSE predictions for $\omega_f \geq 0.10$, and the LST curves underpredict the growth rate due to the neglect of the non-parallelism. Because the growth rate for $\omega_f = 0.05$ is quite low, the agreement between the HLNS and LPSE calculations is expected in further downstream regions. In the region upstream of the neutral point, all the normal modes are damped, but their non-orthogonal nature determines that they could show an algebraic growth, referring to as the non-modal growth. The non-modal growth rate in the leading-edge vicinity oscillates remarkably, indicating the rapid distortion of the perturbation due to the strong non-parallelism. The transition from non-modal perturbation to normal instability mode was also reported by Ricco & Wu (2007). Because the Mack mode is unstable only in travelling wave forms, the boundary-layer response to the FSVD with $\omega_f = 0$ is always non-modal.

Figures 8(a,c,e,g) display the perturbation profiles with $\omega_f = 0$. As x approaches downstream, the amplitudes of $|\tilde{u}_f|$ and $|\tilde{T}_f|$ exhibit significant amplification, while those of $|\tilde{v}_f|$ and $|\tilde{w}_f|$ remain relatively unchanged. This behaviour is a characteristic feature

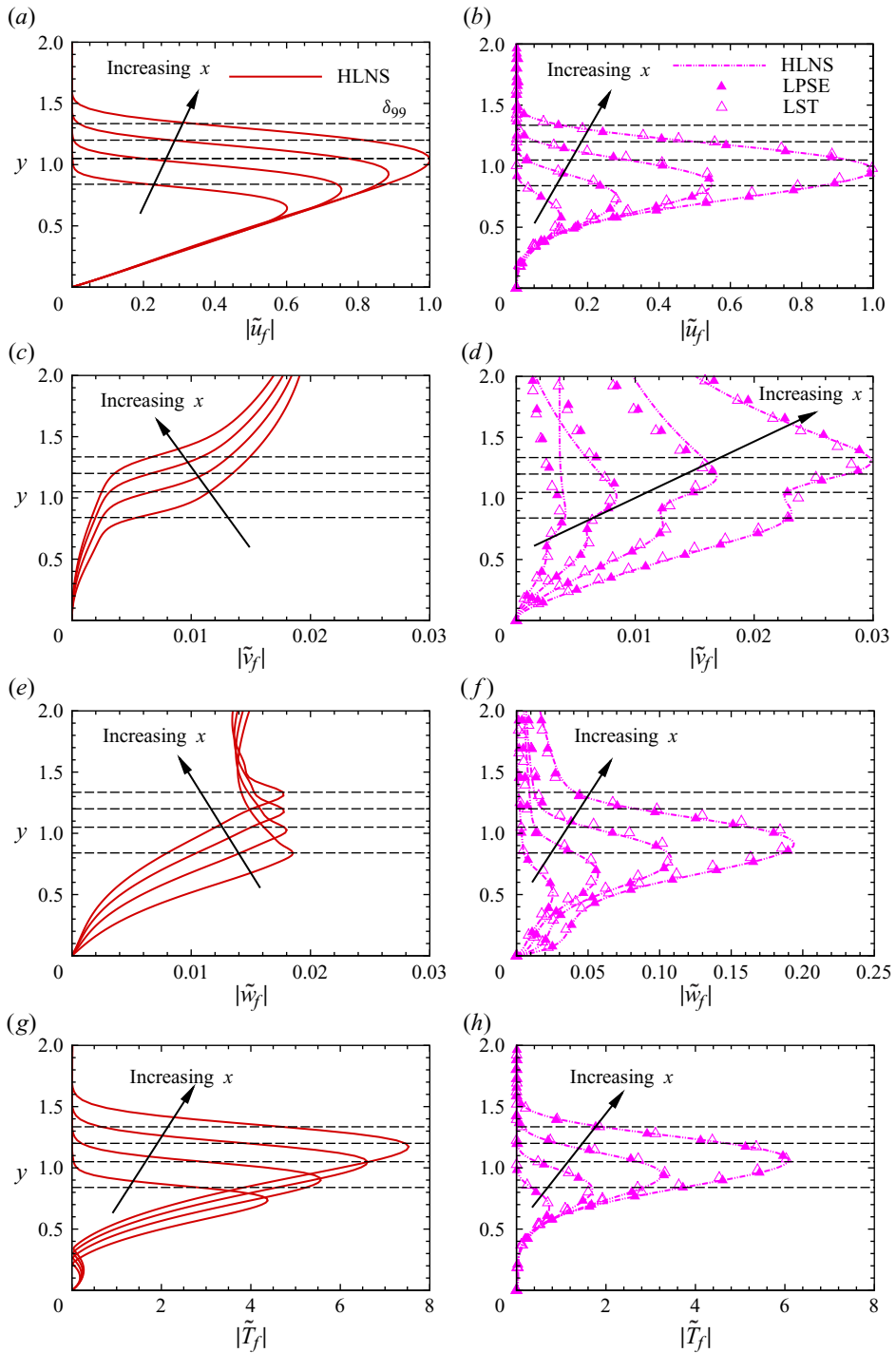


Figure 8. Wall-normal profiles of $|\tilde{u}_f|$, $|\tilde{v}_f|$, $|\tilde{w}_f|$ and $|\tilde{T}_f|$ at $x = 120, 180, 240$ and 300 , where $k_2 = k_3 = 1$, for (a,c,e,g) $\omega_f = 0$, (b,d,f,h) $\omega_f = 0.17$. The results are normalised by the maximum of $|\tilde{u}_f|$ at $x = 300$. The horizontal dashed lines denote the nominal boundary-layer thickness δ_{99} .

of non-modal streaks, where the amplification of \tilde{u}_f and \tilde{T}_f is attributed to the lift-up mechanism. Notably, the peak of the temperature profile is closer to the boundary-layer edge compared to the peak of the \tilde{u}_f profile. In contrast, for $\omega_f = 0.17$, as depicted in figures 8(b,d,f,h), the amplitudes of $|\tilde{u}_f|$, $|\tilde{v}_f|$, $|\tilde{w}_f|$ and $|\tilde{T}_f|$ grow progressively as they propagate downstream. These profiles align with the linear prediction of the Mack first mode obtained by LST, thus confirming the modal nature of the perturbations for $\omega = 0.17$ and $x \geq 120$.

Figure 9(a) summarises the variation of the perturbation amplitude \tilde{U}_f with ω_f at different streamwise locations for $k_3 = 0.33$ and $\Theta = 45^\circ$. At $x = 30$ and 60 , \tilde{U}_f decreases monotonically with increase of ω_f , and the amplitude is greater in a downstream position. As x increases to 120 , the amplitude shows a local peak at around $\omega_f = 0.02$, and decreases with ω_f for higher frequencies. When $x = 240$, the amplitude shows a local minimum (marked by a circle) at around $\omega_f = 0.03$, and for higher ω_f values, the curve shows the same feature as that for $x = 120$. Comparing the \tilde{U}_f curves with the LST predictions, we find that the local minimum point can be viewed as a critical frequency distinguishing the normal and non-modal growth of each perturbation at one location. Changing the wavenumbers k_3 and keeping $\Theta = 45^\circ$, we plot \tilde{U}_f in figures 9(b), 9(c) and 9(d), and similar trend is observed. For the same k_3 , the transition from non-modal to modal perturbations appears earlier as ω_f increases, and at the same position, the critical frequency increases with k_3 .

3.4. *Linear response of a boundary layer to a spanwise vibration*

For a weak wall vibration without any FSVD, the boundary-layer response $\tilde{\varphi}_s$ is obtained by solving (2.4) numerically. Only \tilde{w}_s is non-zero, and its profiles for $\omega_s = 0.05$ at different streamwise locations are shown in figure 10(a). As expected, the perturbation peaks at the wall, and attenuates as the boundary-layer edge is approached. Neglecting the non-parallelism, the lateral velocity perturbation can be approximated by the Stokes layer solution $\mathcal{E}_s W_{Stokes} \exp(-i\omega_s t) + \text{c.c.}$, where

$$W_{Stokes}(y) = \exp((-i\omega_s R)^{1/2}y), \tag{3.1}$$

with $-i$ chosen to be $\exp(3\pi i/2)$. The comparison of \tilde{w}_s at $x = 240$ with W_{Stokes} is plotted in figure 10(b), showing a good agreement.

3.5. *The HWNNS calculations for the perturbations excited by FSVD–vibration interaction*

As suggested by (2.3), the perturbation field for a vibration configuration includes $\tilde{\varphi}_f$, $\tilde{\varphi}_s$ and $\tilde{\varphi}_\pm$. The streamwise velocity and temperature amplitudes of $\tilde{\varphi}_\pm$ are denoted by $\tilde{U}_\pm(x) = \max_y(|\tilde{u}_\pm(x, y)|)$ and $\tilde{T}_\pm(x) = \max_y(|\tilde{T}_\pm(x, y)|)$, respectively. Actually, there would be more perturbations excited by the higher-order interactions, such as the perturbation with frequencies $2\omega_s + \omega_f$ and $\omega_s + 2\omega_f$, which are neglected in this subsection due to their smaller magnitudes. The resolution study for the HWNNS calculations is provided in figure 29(a) in Appendix A, and its comparison with the DNS result is provided in figure 30 in Appendix B.

For different vibration amplitudes, figures 11(a) and 11(b) display the evolutions of \tilde{U}_f and \tilde{T}_f obtained by HWNNS, respectively. All the curves follow the same trend as the non-vibration curve (red solid lines), i.e. increase drastically in the close neighbourhood

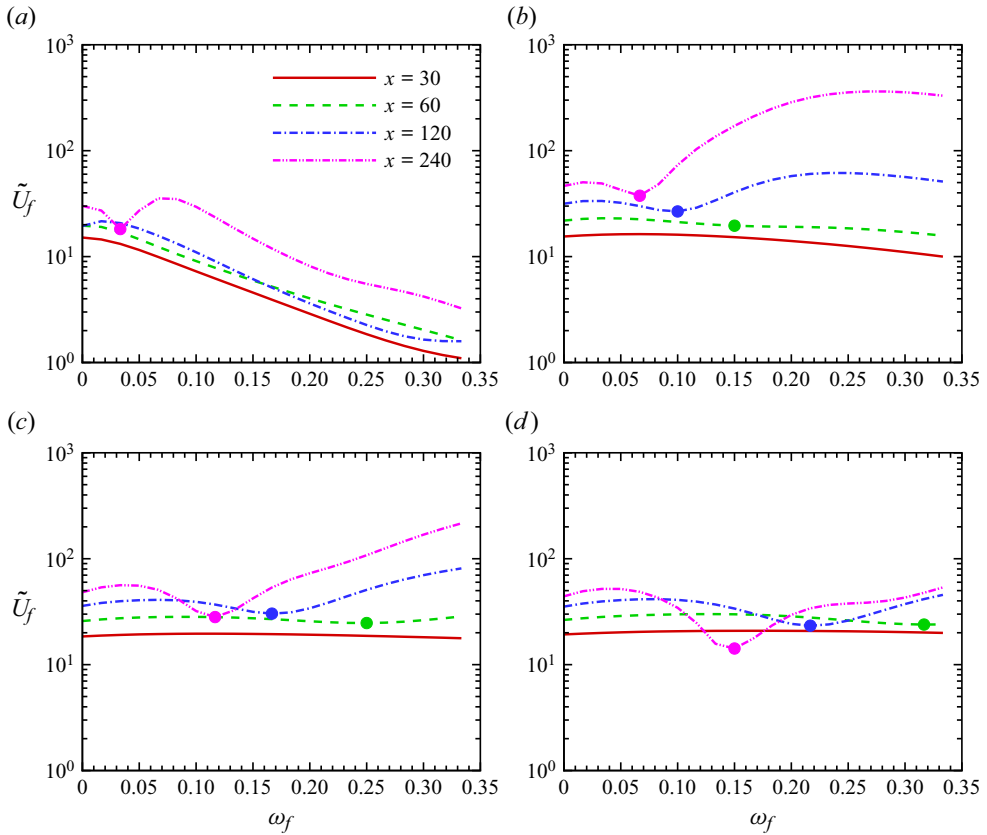


Figure 9. Amplitudes of the excited perturbations with $\Theta = 45^\circ$ at different locations, where the circles mark the critical frequency distinguishing the non-modal and modal perturbations, for (a) $k_3 = 0.33$, (b) $k_3 = 1$, (c) $k_3 = 2$, (d) $k_3 = 2.67$.

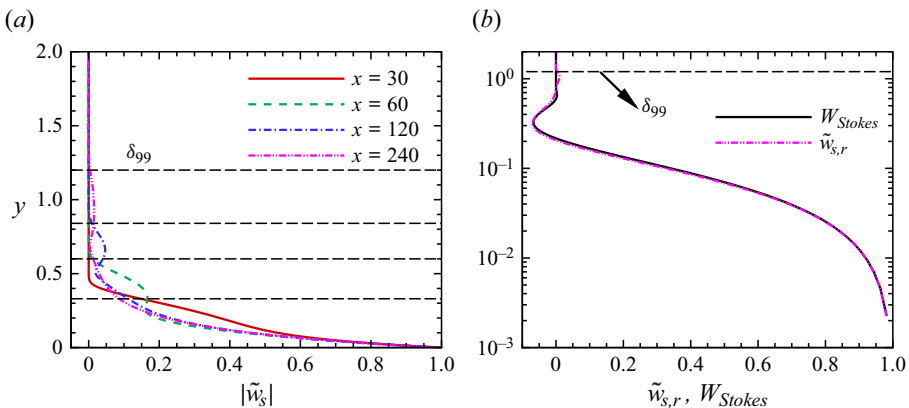


Figure 10. (a) Wall-normal profiles of $|\tilde{w}_s|$ at different stations with $\omega_s = 0.05$. (b) Comparison of $\tilde{w}_{s,r}$ for $x = 240$ with W_{Stokes} .

of the leading edge, followed by mild decreases, and then increase gently with x until the end of the calculations. Again, \tilde{T}_f is more than one order of magnitude higher than \tilde{U}_f . Remarkably, inclusion of the surface vibration leads to a reduction of the amplitudes \tilde{U}_f and \tilde{T}_f in the downstream region, and such a reduction strengthens as the vibration intensifies, indicating a suppression of the FSVD-induced streak. Such an observation agrees with that of Hicks & Ricco (2015). Figures 11(c) and 11(d) show the evolution of \tilde{U}_\pm and \tilde{T}_\pm , respectively, and a monotonic increase with x is observed for each curve. As expected, a stronger vibration results in a greater amplitude of \tilde{U}_\pm or \tilde{T}_\pm in the downstream region, and at the same location, \tilde{U}_+ (\tilde{T}_+) is greater than \tilde{U}_- (\tilde{T}_-). A clearer measurement of the excited mode \tilde{U}_\pm is to normalise them by \tilde{U}_f at each x location, namely,

$$\tilde{A}_\pm(x) \equiv \tilde{U}_\pm(x)/\tilde{U}_f(x). \quad (3.2)$$

The evolution of \tilde{A}_\pm for different \mathcal{E}_s is shown in figures 11(e) and 11(f). Overall, each curve shows a sharp increase in the leading-edge vicinity ($x < 40$), followed by a mild variation, including an almost constant state in the downstream limit of \tilde{A}_- and an increase with x of \tilde{A}_+ . Increase of \mathcal{E}_s leads to higher values of \tilde{A}_\pm , and for $\mathcal{E}_s = 0.03$, the value of \tilde{A}_+ can even reach unity, indicating a strong distortion of the FSVD-induced streaks. If the wave angle Θ of the FSVD were changed from 45° to -45° , then the evolution curves of \tilde{U}_+ and \tilde{U}_- would swap.

Increasing the frequency of the FSVD to $\omega_f = 0.17$, the streamwise evolutions of the perturbations, shown in figure 12, are similar to those for the stationary-FSVD configuration shown in figure 11. However, the amplification rates of \tilde{U}_f and \tilde{U}_\pm in the downstream region are much greater, because the perturbations at these frequencies enter the unstable region of the Mack first mode. Comparing the results for different vibration amplitudes, it is found that in the region $x < 100$, the vibration suppresses the FSVD-induced perturbation \tilde{U}_f , but a destabilising effect is observed in further downstream locations where the perturbation is the Mack mode. The implication is that the lateral vibration would suppress the non-modal perturbations but enhance the modal perturbations.

In figure 13, we probe the behaviours of \tilde{U}_f and \tilde{U}_+ by varying ω_f , k_3 and Θ . Comparing figure 13(a) to figure 9(b), we find that the vibration impact on the FSVD-induced perturbation at this \mathcal{E}_s value is rather limited, and again, the minima of the \tilde{U}_f curves indicate the critical frequency distinguishing the non-modal and modal perturbations. In contrast, the amplitudes \tilde{U}_+ in the downstream locations do not show local minima, as shown in figure 13(d). To avoid the transition of \tilde{U}_f from non-modal to modal perturbations and perform a clear investigation of the bypass transition, we select $\omega_f = 0$ in the following. It is seen from figures 13(b,e) that \tilde{U}_f and \tilde{U}_+ show broad peaks at a downstream location $x = 240$ in a region around $k_3 = 1.4$. Setting $k_3 = 1$ and $\omega_f = 0$, we plot the dependence of \tilde{U}_f and \tilde{U}_+ on the wave angle $\Theta = \tan^{-1}(k_2/k_3)$ in figures 13(c,f), respectively. It should be noted that an FSVD with both $\omega_f = 0$ and $k_2 = 0$ is not possible from the dispersion relation (2.9), so the curves in the close neighbourhood of $\Theta = 0$ are not shown. Apparently, the boundary-layer response to both FSVD and vibration is stronger when the wave angle Θ is small. Therefore, in order to achieve a relatively high boundary-layer response, we choose $\omega_f = 0$, $k_3 = 1$ and $\Theta = 15^\circ$ in the following nonlinear calculations.

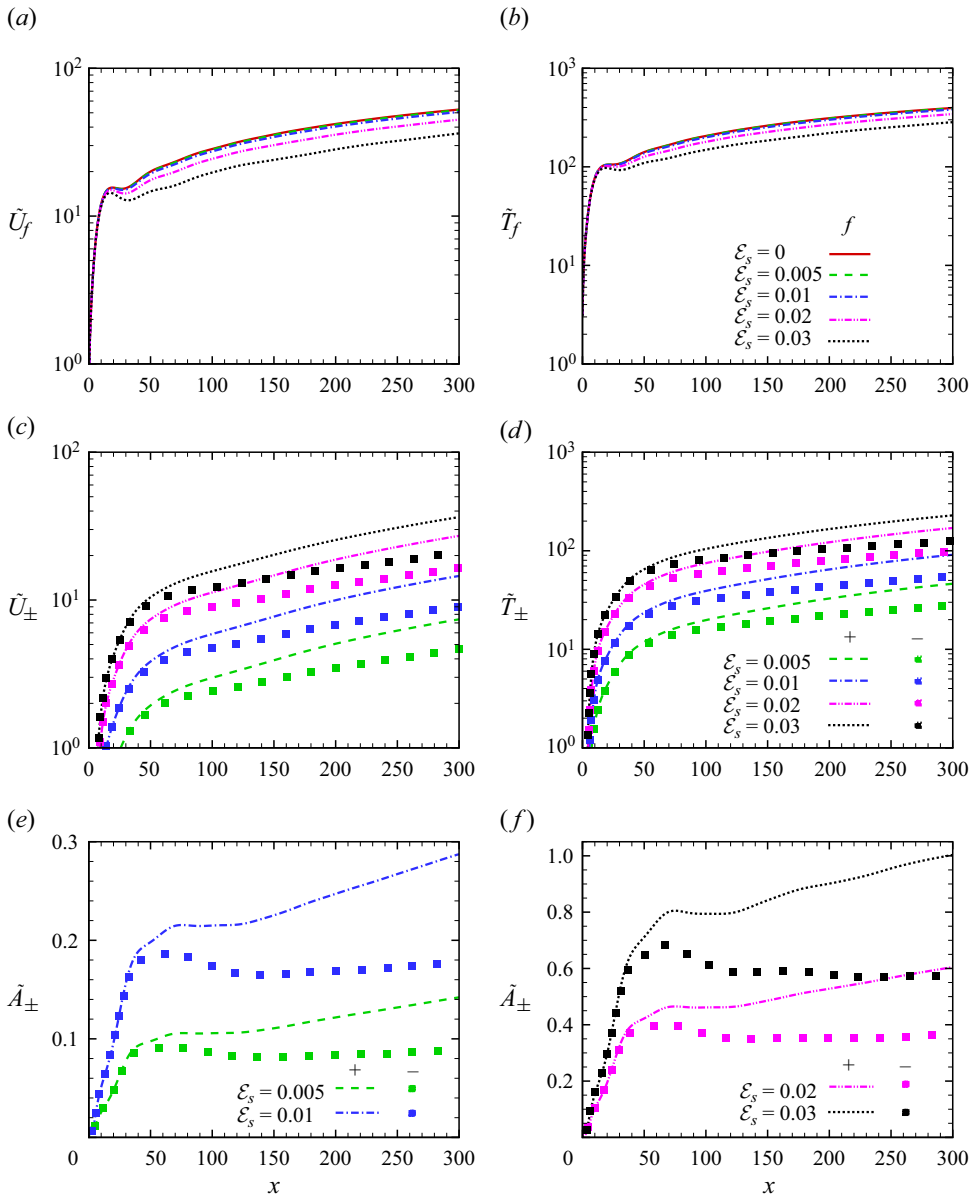


Figure 11. Streamwise evolution of (a) \tilde{U}_f , (b) \tilde{T}_f , (c) \tilde{U}_\pm , (d) \tilde{T}_\pm , and (e, f) $\tilde{A}_\pm \equiv \tilde{U}_\pm/\tilde{U}_f$, where $k_3 = 1$, $\Theta = 45^\circ$, $\omega_s = 0.05$ and $\omega_f = 0$.

4. Nonlinear evolution of the streaks and their SI

4.1. Nonlinear evolution of the streaks excited by FSVD–vibration interaction

As shown in the previous section, the vibration modulates perturbations \tilde{U}_\pm with frequencies different from that of the FSVD-induced streak, and influences the amplitude evolution of the latter. If the amplitude of the FSVD \mathcal{E}_f is moderate, then the nonlinearity would not be negligible in the downstream region. In this subsection, we will perform NPSE calculations for the nonlinear evolution of the boundary-layer perturbations.

Influence of wall vibration on non-modal perturbations

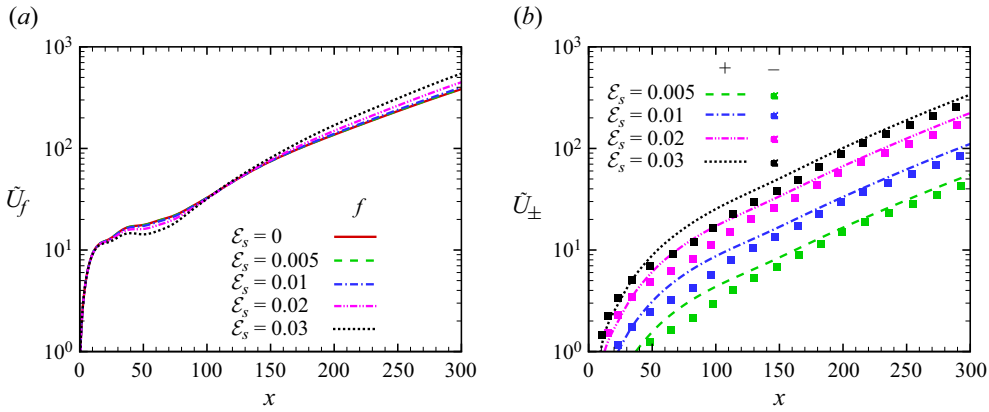


Figure 12. Streamwise evolution of \tilde{U}_f and \tilde{U}_{\pm} for $k_3 = 1$, $\Theta = 45^\circ$ and $\omega_f = 0.17$.

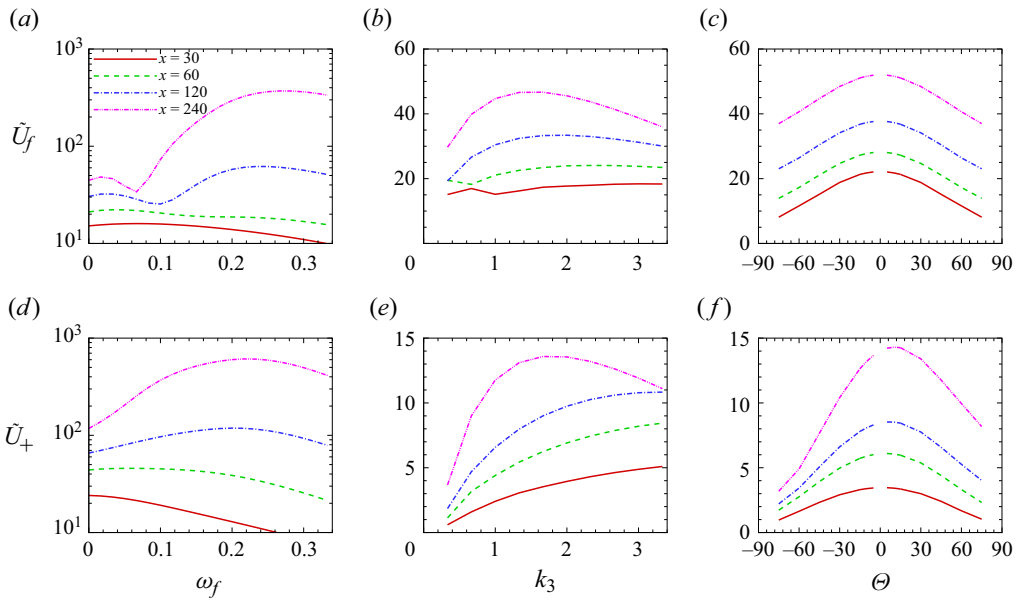


Figure 13. Streamwise evolution of (a–c) \tilde{U}_f and (d–f) \tilde{U}_{\pm} for $\omega_s = 0.05$ and $\mathcal{E}_s = 0.01$: (a,d) dependence on ω_f for $k_3 = 1$ and $\Theta = 45^\circ$; (b,e) dependence on k_3 for $\omega_f = 0$ and $\Theta = 45^\circ$; (c,f) dependence on Θ for $\omega_f = 0$ and $k_3 = 1$.

The NPSE calculation starts from $X_0 = 60$, where the base flow already satisfies the self-similarity solution, and the inflow perturbations are obtained by the aforementioned HWNNs calculations. In the physical situation, the vibration frequency is usually low, so the FSVDs with lower frequencies play a more important role. Thus, for demonstration, we choose the frequency of the FSVD ω_f to be zero; the perturbation evolution with sufficiently low \mathcal{E}_f values was shown in figure 11. In NPSE calculations, we choose $(\mathcal{M}, \mathcal{N}) = (5, 5)$, which has been confirmed to be sufficiently accurate as compared with the results with $(\mathcal{M}, \mathcal{N})$ doubled. The mesh resolution study of the NPSE can be found in figure 29(b) in Appendix A, and the comparison of the HWNNs + NPSE calculations with DNS is provided in figure 31 in Appendix B.

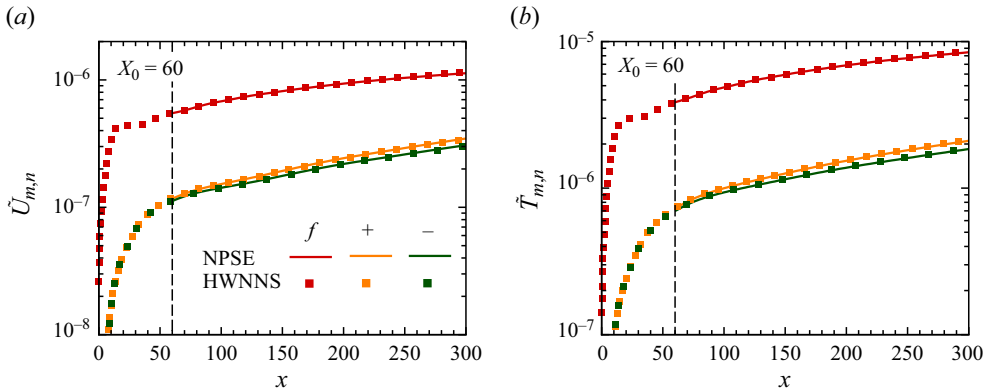


Figure 14. Evolution of the perturbation amplitudes (a) $\tilde{U}_{m,n}$ and (b) $\tilde{T}_{m,n}$ for $\omega_f = 0$, $\mathcal{E}_f = 10^{-8}$, $k_3 = 1$, $\Theta = 15^\circ$, $\omega_s = 0.05$ and $\mathcal{E}_s = 0.01$.

We first choose $\mathcal{E}_f = 10^{-8}$ and perform a comparison between the HWNNS and NPSE calculations to confirm the consistency of our numerical results. The controlling parameters are $\omega_s = 0.05$, $\mathcal{E}_s = 0.01$, $\omega_f = 0$, $k_3 = 1$ and $\Theta = 15^\circ$. The amplitudes of $\tilde{U}_{m,n}(x) = \max_y(\mathcal{E}_{m,n} |\tilde{u}_{m,n}(x, y)|)$ and $\tilde{T}_{m,n}(x) = \max_y(\mathcal{E}_{m,n} |\tilde{T}_{m,n}(x, y)|)$ obtained by the two approaches are shown in figure 14. Here, (m, n) denotes a Fourier mode with frequency $m\omega_s$ and spanwise wavenumber nk_3 . Both the entrainment of the vortical perturbation $(0, 1)$ and its interaction with the surface vibration $(\pm 1, 1)$ obtained by the two approaches agree perfectly. The agreement of the perturbation profiles at $x = 300$, as shown in figure 15, is also achieved.

For the calculations of the nonlinear evolution, we choose five groups of controlling parameters with different vibration amplitudes \mathcal{E}_s as shown in table 2. In this subsection, we let the FSVDs consist of a pair of oblique stationary vortical perturbations with opposite wall-normal wavenumbers $\pm k_2$:

$$\mathcal{E}_f (\hat{\phi}_{f,+} \exp(i(k_2y + k_3z)) + \hat{\phi}_{f,-} \exp(i(-k_2y + k_3z))) + \text{c.c.} \quad (4.1)$$

Such a selection ensures the symmetric feature about the $y = 0$ plane. Note that although the FSVD amplitudes \mathcal{E}_f in table 2 are chosen to be as small as 0.0005, the superposition of the four Fourier components (including $\hat{\phi}_{f,+}$, $\hat{\phi}_{f,-}$ and their complex conjugates) determines the physical amplitude of the FSVD to be 0.002. The boundary-layer responses to the FSVDs are denoted by $\tilde{\phi}_{f,\pm}(x, y) \exp(ik_3z)$, and the two components together show a longitudinal streak feature in the boundary layer.

Figure 16(a) plots the streamwise evolution of $\tilde{U}_{m,n}$ of the representative Fourier modes excited by the FSVDs for case A. Because \mathcal{E}_f is not large, the excited streak mode $(0, 1)$ calculated by NPSE (marked by the red solid line) agrees well with the prediction given by the HWNNS approach (marked by the squares) or the LPSE (marked by the circles). However, the NPSE has the capability to predict the evolution of higher-order harmonics, such as $(0, 2)$, $(0, 3)$, and so on, as well as the mean-flow distortion (MFD) $(0, 0)$. Initially, these components are taken to be zero at the inlet due to their small magnitudes. However, they are excited in the downstream region due to nonlinearity. This mismatch results in a kink in each curve near the inlet, but it does not affect the downstream NPSE calculations since different choices of X_0 yield the same downstream perturbation field. The harmonic streak mode $(0, 2)$ and MFD $(0, 0)$ are generated through the self-interaction of $(0, 1)$ or the mutual interaction of $(0, \pm 1)$, which grow with a rate twice of that of $(0, 1)$ in

Influence of wall vibration on non-modal perturbations

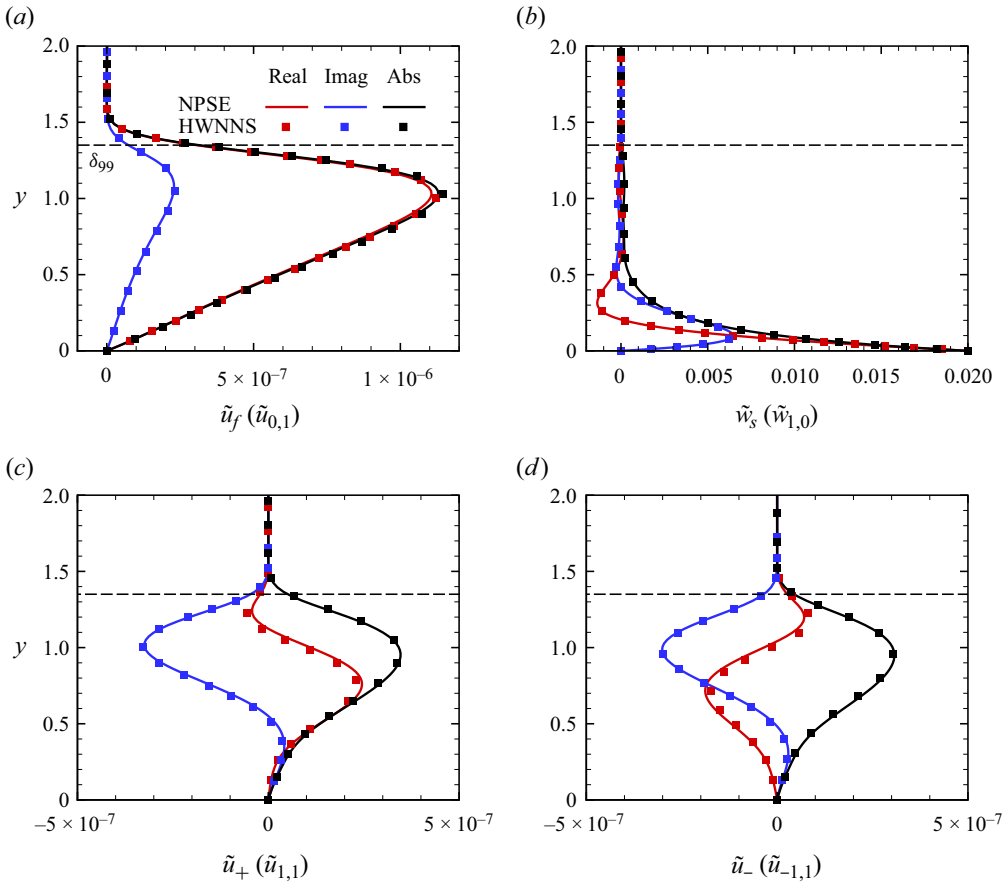


Figure 15. Wall-normal profiles of (a) \tilde{u}_f , (b) \tilde{w}_s , (c) \tilde{u}_+ and (d) \tilde{u}_- at $x = 300$. The parameters are the same as in figure 14.

Case	ω_f	k_3	Θ	\mathcal{E}_f	ω_s	\mathcal{E}_s
A	0	1	15°	0.0005	0	0
B	0	1	15°	0.0005	0.05	0.005
C	0	1	15°	0.0005	0.05	0.01
D	0	1	15°	0.0005	0.05	0.02
E	0	1	15°	0.0005	0.05	0.03

Table 2. Parameters for perturbations for the nonlinear calculations.

the downstream region, with the former being stronger. For the vibrating wall cases, as shown in figures 16(b–e), because of the additionally introduced perturbation (1, 0), the Fourier modes $(\pm 1, 1)$ are excited. Overall, the NPSE calculations of $(\pm 1, 1)$ and $(0, 1)$ are smaller than the HWNNS calculations in the region $x > 120$, and the discrepancy enlarges as the vibration intensifies. Comparing the evolution of the streak mode $(0, 1)$ for different cases, it is again seen that the stabilising effect of the vibration on the streak mode is evident, and the amplitudes of $(\pm 1, 1)$ even exceed the FSVD-induced perturbation $(0, 1)$ in downstream locations for case E. The implication is that for this

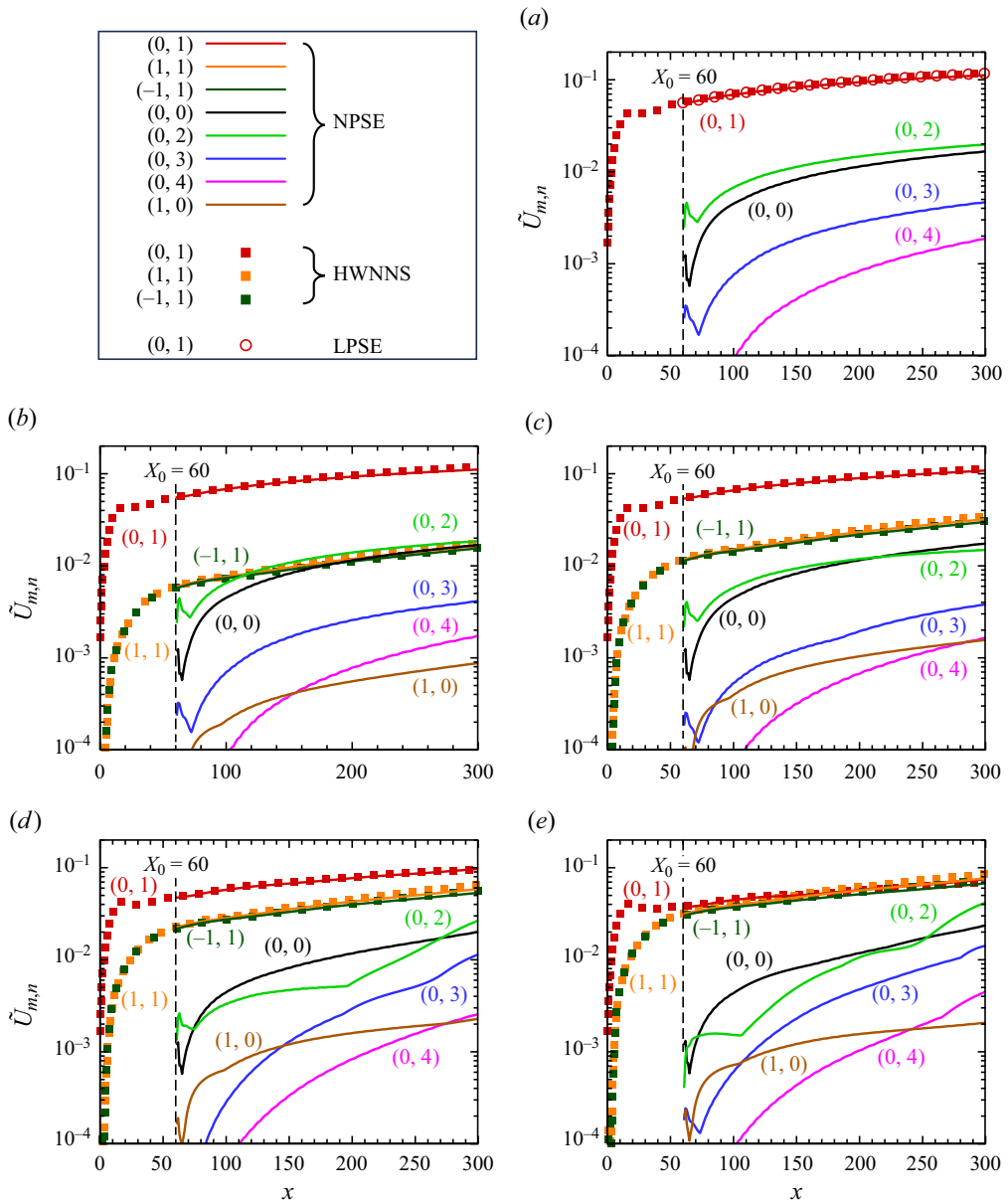


Figure 16. Nonlinear evolution of the amplitude of the boundary-layer perturbations $\tilde{U}_{m,n}$ for $\omega_f = 0$ and $\omega_s = 0.05$, where (a–e) show cases A–E.

case, the streaky structure is strongly influenced by the vibration, which could alter its SI. This phenomenon was also reported in many papers for incompressible flows (Hack & Zaki 2014, 2015; Hicks & Ricco 2015). Since the amplitudes of the components (0, 2) and (0, 0) have reached $O(0.01)$ in the downstream region for all cases considered, their influence on the streaky structure and its instability property is non-negligible, as will be studied in the next subsection.

Influence of wall vibration on non-modal perturbations

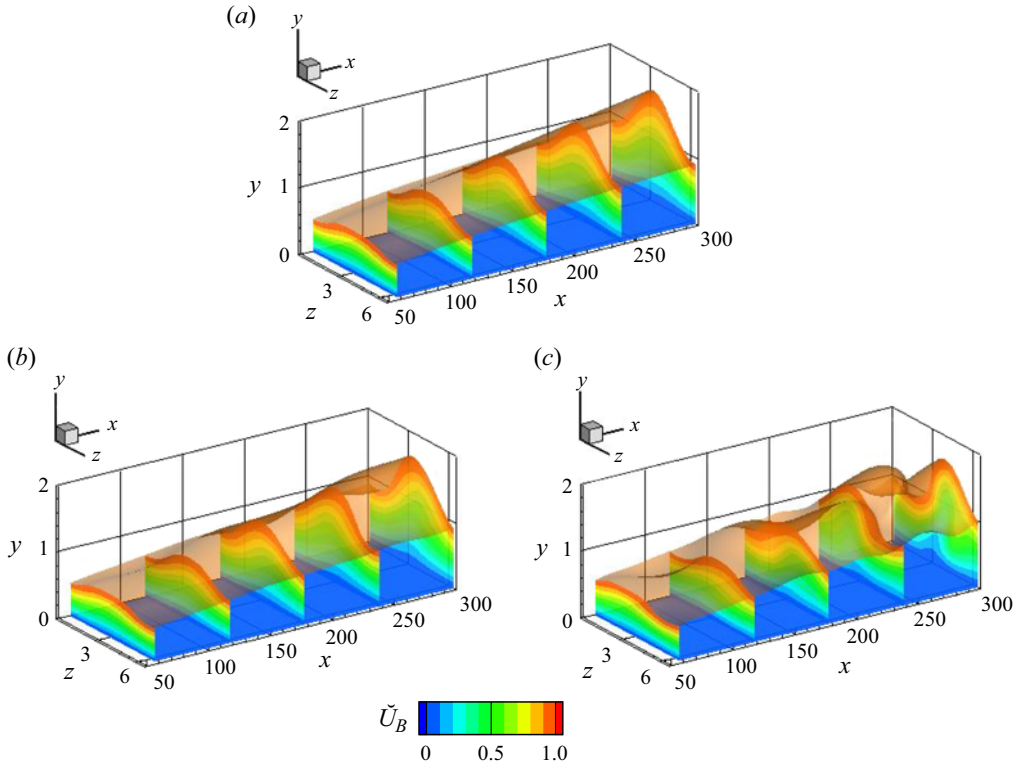


Figure 17. Contours of the streamwise velocity \check{U}_B of the streaky base flow: (a) case A; (b) case C with $t = 0$; (c) case E with $t = 0$.

4.2. The SI analysis

The streaks do not break down themselves, but they could support SI modes with higher growth rates, which can be analysed by the numerical approach in § 2.6.

4.2.1. The SI analysis for case A

For case A, the streak is stationary with a long streamwise length scale compared to the SI wavelength, and the SI analysis can be performed at a chosen x position based on the parallel-flow assumption. Figure 17(a) shows the streaky structure obtained by the NPSE calculation, where the spanwise domain size is set to be one wavelength of the FSVD, $2\pi/k_3 \approx 6.28$. As x approaches downstream, the mean velocity \check{U}_B shows stronger gradients in both the spanwise and wall-normal directions.

The temporal SI analysis is performed by solving (2.14) numerically. The growth rates ω_i of the most unstable varicose and sinuous modes at three streamwise locations are shown in figure 18(a). The perturbation profiles of representative varicose and sinuous modes at $x = 300$ are displayed in figure 19, showing a symmetric and an anti-symmetric feature along the centreline, respectively. For the base-flow profiles concerned here, the varicose mode is overall more unstable. At each streamwise location, the unstable zone shows two peaks, and the one with a higher wavenumber is more unstable. This is a reminiscent of the Mack mode instability for a Blasius base flow, but the instability property is modified quantitatively by the streaks. As x approaches downstream, the peak value of the second lobe decreases mildly, with its corresponding wavenumber shifted to a lower value.

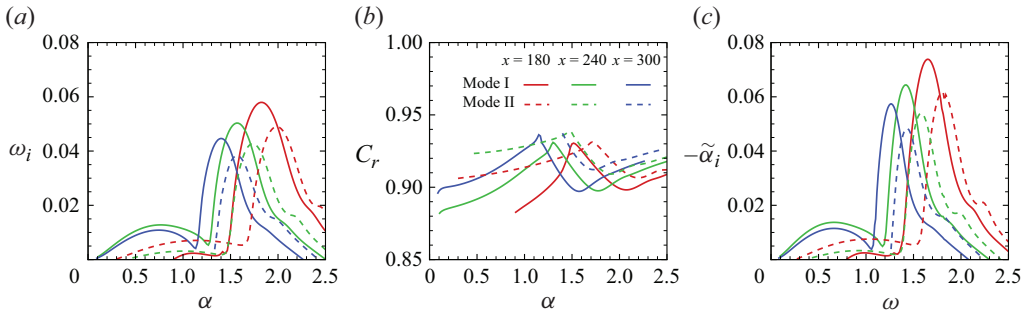


Figure 18. Dependence on α of (a) the temporal growth rate ω_i , (b) the phase speed C_r and (c) the spatial growth rate $-\tilde{\alpha}_i$, of representative unstable SI modes for case A.

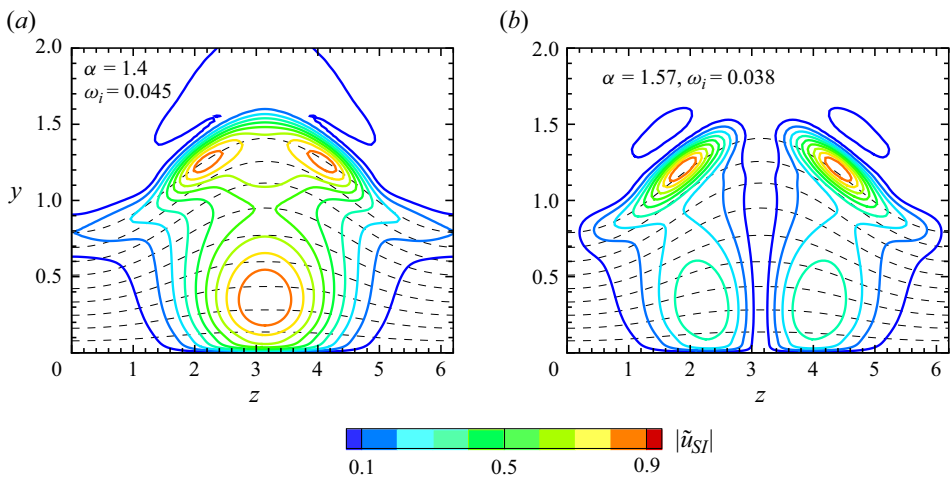


Figure 19. Eigenfunctions of $|\tilde{u}_{SI}|$ at $x = 300$ for case A: (a) mode I for $\alpha = 1.4$; (b) mode II for $\alpha = 1.57$. The dashed lines represent the contours of the base flow \tilde{U}_B .

The phase speeds C_r , shown in figure 18(b), vary in the region (0.88, 0.94), indicating an inviscid nature of the SI modes. Using the Gaster transformation (Gaster 1962; Xu *et al.* 2023), we are able to convert the temporal growth rate to the spatial growth rate via

$$\tilde{\alpha} = \tilde{\alpha}_r + i\tilde{\alpha}_i = (\alpha - \omega_i \sin \vartheta / |C_g|) - i(\omega_i \cos \vartheta / |C_g|), \quad (4.2)$$

where $C_g \equiv |C_g| \exp(i\vartheta) \equiv \partial\omega/\partial\alpha$ is the complex group velocity. The spatial growth rate $-\tilde{\alpha}_i$ is plotted in figure 18(c), and a feature similar to that in figure 18(a) is evident.

The accumulated amplitude of a linear perturbation can be predicted by an N -factor, defined by

$$N(x) = \int_{x_1}^x -\tilde{\alpha}_i(x) dx, \quad (4.3)$$

where x_1 denotes the neutral location of the unstable perturbation. Based on the spatial growth rates $-\tilde{\alpha}_i$ shown in figure 20(a), the N -factors for different ω values are shown in figure 20(b). For $\omega \leq 1.17$, the N -factor grows gently with x until the end of the calculation, and the greatest value of the N -factor is 4.49, appearing for $\omega = 0.5$ at $x = 300$. For a higher ω value, the N curve undergoes a sharp increase at a certain position,

Influence of wall vibration on non-modal perturbations

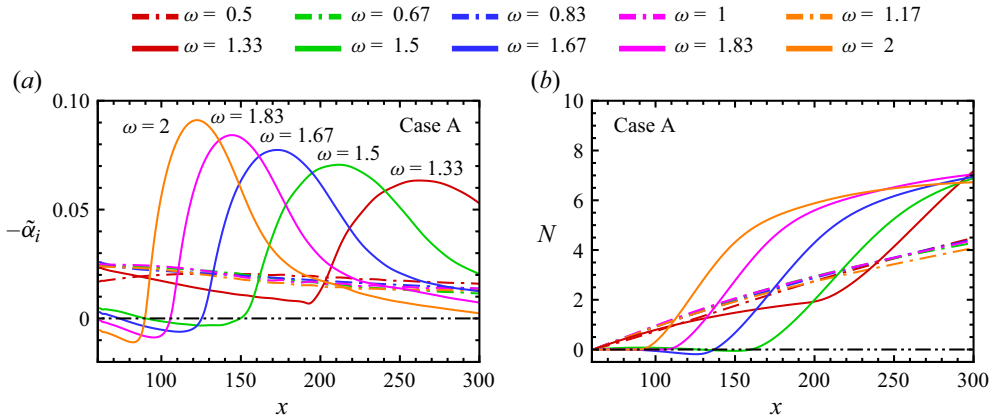


Figure 20. Evolution of (a) spatial growth rates $-\tilde{\alpha}_i$ and (b) N -factors of the SI modes for different frequencies predicted by SI analysis for case A. The dash-dot-dotted lines denote the zero value.

due to the appearance of the second peak of the varicose mode. This sharp increase moves upstream as ω increases, agreeing with the peaks of the growth rates shown in figure 20(a).

4.2.2. The SI analysis for cases with vibrating walls

For a vibrating wall, because the excited streaks vary with longer time and length scales than the SI modes, the SI analysis should be performed at a frozen time and streamwise location. Two snapshots of the streaky structure of cases C and E at $t = 0$ are shown in figures 17(b) and 17(c), respectively. Figures 21(b), 21(c) and 21(d) further show the contours of the unsteady streaky base flow at $x = 300$ at different time instants for case C, and the base flow for case A is also shown in figure 21(a) for comparison. Here, the vibrating period is defined as $T_s = 2\pi/\omega_s$. The distortion of the streaky base flow by the unsteady vibration at different phases is clearly displayed.

The growth rates of the SI modes for the base flow shown in figure 21 are compared in figure 22. Because the base flow for case C is not symmetric along the centreline, it is not possible to define the varicose and sinuous modes. Therefore, we denote the two most unstable modes by mode I and mode II. For case C at $t = T_s/4$, the growth rate for the most unstable wavenumber band is quite close to that for case A. The vibration leads to a slight destabilising and stabilising effects on modes I and II, respectively. The instability properties for $t = 0$ and $T_s/2$ are almost the same, for which both modes I and II have greater growth rates in a wide wavenumber band, except in a local region around the peaks of the two modes for case A. For case E, because the streaky structure is severely influenced by the vibration, more SI modes with greater growth rates can be found, and figure 23 displays only the most unstable two or three modes at different time instants. The destabilising effect due to the vibration is evident for the whole wavenumber band. The eigenfunctions of the most unstable modes for cases C and E are shown in figure 24. For all the plots, the eigenfunctions peak at the localised region around the shoulder of the skewed mushroom-type structure where the shear is strong.

For an unsteady streaky base flow, the amplitude accumulation should be calculated in a more complicated way than that for case A, i.e. the integral path of the N -factor should follow the trajectory of the group velocity of the SI mode. The premise is that the variation of the streaky base flow is in a much longer length scale than the wavelength of the SI mode. Denote the SI growth rate at a time t and a location x as $-\tilde{\alpha}_i(x, t)$. Then the

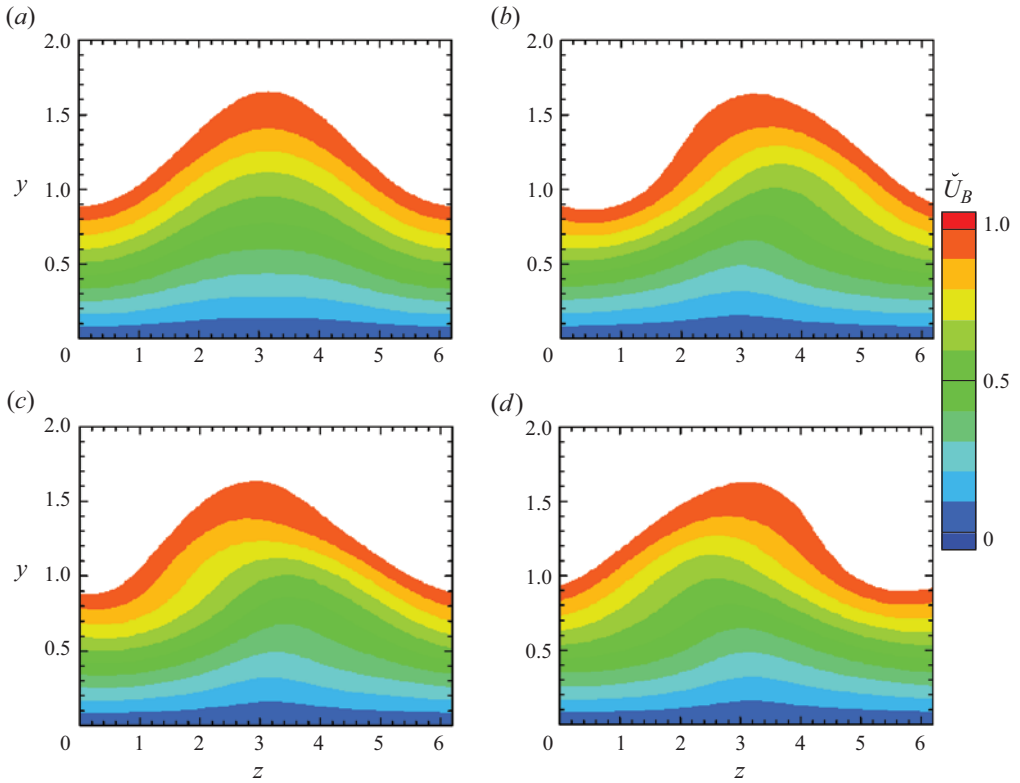


Figure 21. Contours of the instant streamwise velocity \tilde{U}_B of the unsteady streaky base flow at $x = 300$: (a) case A; (b) case C at $t = 0$; (c) case C at $t = T_s/4$; (d) case C at $t = T_s/2$.

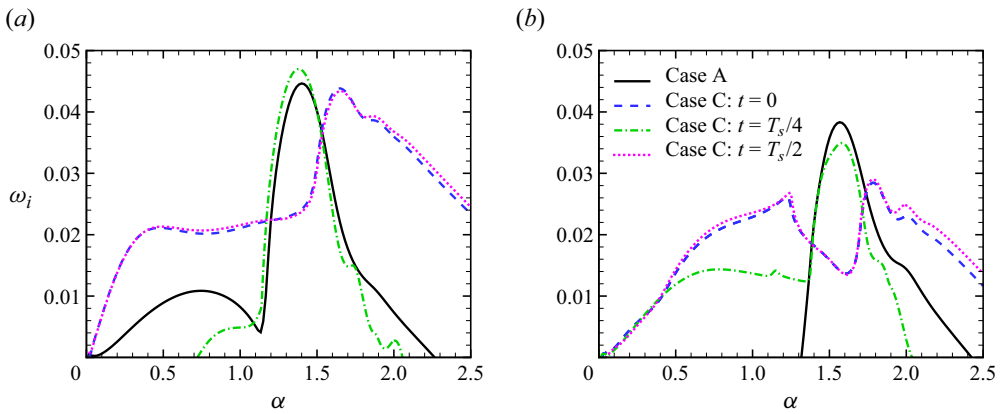


Figure 22. Dependence on α of the temporal growth rate ω_i of representative unstable SI modes for case C at $x = 300$, where the result for case A is also shown for reference: (a) mode I, (b) mode II.

N -factor can be calculated by

$$N(x, \bar{t}_0) = \int_{x_1}^x -\tilde{\alpha}_i(\bar{x}, \bar{t}_0 + \bar{x}/C_{g,r}) d\bar{x}, \quad (4.4)$$

Influence of wall vibration on non-modal perturbations

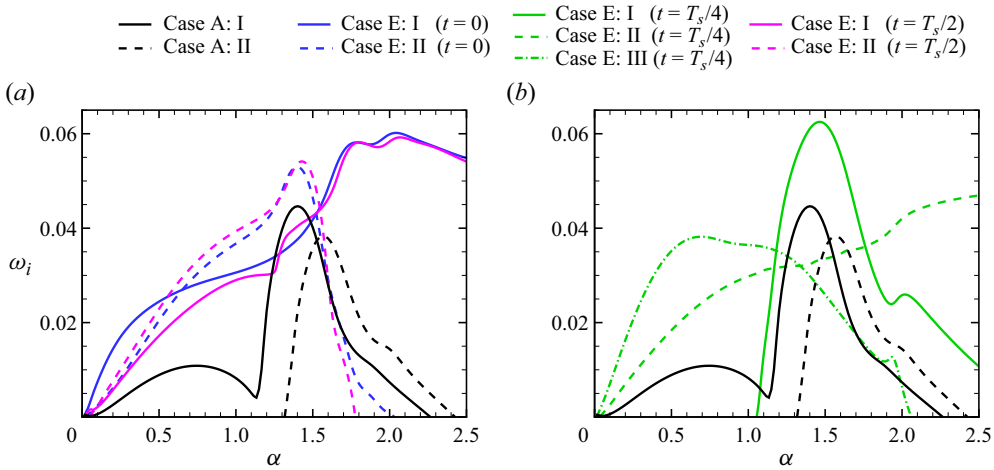


Figure 23. Dependence on α of the temporal growth rate ω_i of representative unstable SI modes for case E at $x = 300$, where the result for case A is also shown for reference: (a) $t = 0$ and $T_s/2$; (b) $t = T_s/4$.

where $C_{g,r}$ denotes the group velocity of the SI mode, and \bar{t}_0 is the initial time instant t_0 distinguishing the initial phase. In figure 25, we show one example of the calculation strategy for $\omega = 1.33$ for case C. First, we plot the growth rate contours in the $x-t$ plane in figure 25(a), where the results for five time periods are shown. The growth rate shows an appreciable variation for different phases within one period, but overall it shows a broad peak in the interval $x \in (210, 300)$. The contours of the group velocity are shown in figure 25(b), which shows a peak at $x \approx 195$, but becomes smaller at further downstream positions. The propagation trajectories of the SI modes in the $x-t$ plane are shown by the arrowed lines, which are the basis for the calculations of the N -factor starting from different phases. In figure 25(c), the dependence on x of the growth rates along the 16 trajectories is shown by the grey curves, with their averaged value marked by the red dashed line. For comparison, the result for case A is plotted by the black line. For $x < 180$, the effect of vibration on the SI growth is a little stabilising, but a destabilising effect is evident for most of the initial phases in further downstream locations. Integrating $-\tilde{\alpha}_i(\bar{x}, \bar{t}_0 + \bar{x}/C_{g,r})$ along \bar{x} , we obtain the N -factor for different initial phases \bar{t}_0 , as shown in figure 25(d). It is seen that at this frequency, the evolution of the averaged N -factor for case C is rather close to that of case A, but the instantaneous N -factor scatters in the downstream region, showing an intermittent feature of the accumulated SI perturbations.

In figure 26, we examine the evolution of the growth rate and the N -factor for two other representative frequencies. Among the 16 curves starting from different initial instants, we choose the two with the maximum and minimum values of the N -factor at $x = 300$, shown by the dashed and dotted lines. The time-averaged values are also shown by the curves with circles. As shown in figures 26(a,c), the growth rate for each case fluctuates in the downstream region, but the averaged growth rate is overall suppressed by the vibration for $\omega = 0.83$, and enhanced by the vibration for $\omega = 2$. Integrating the growth rate along x , we obtain the evolution of the N -factors in figures 26(b,d). As expected, the averaged N -factor in the downstream region is reduced for a low frequency, but is increased for a high frequency. Since the high-frequency perturbations attain a greater N -factor, they may be more important on triggering the bypass transition. Additionally, comparing the results for cases C and D, it is found that a stronger vibration leads to a greater increment of the

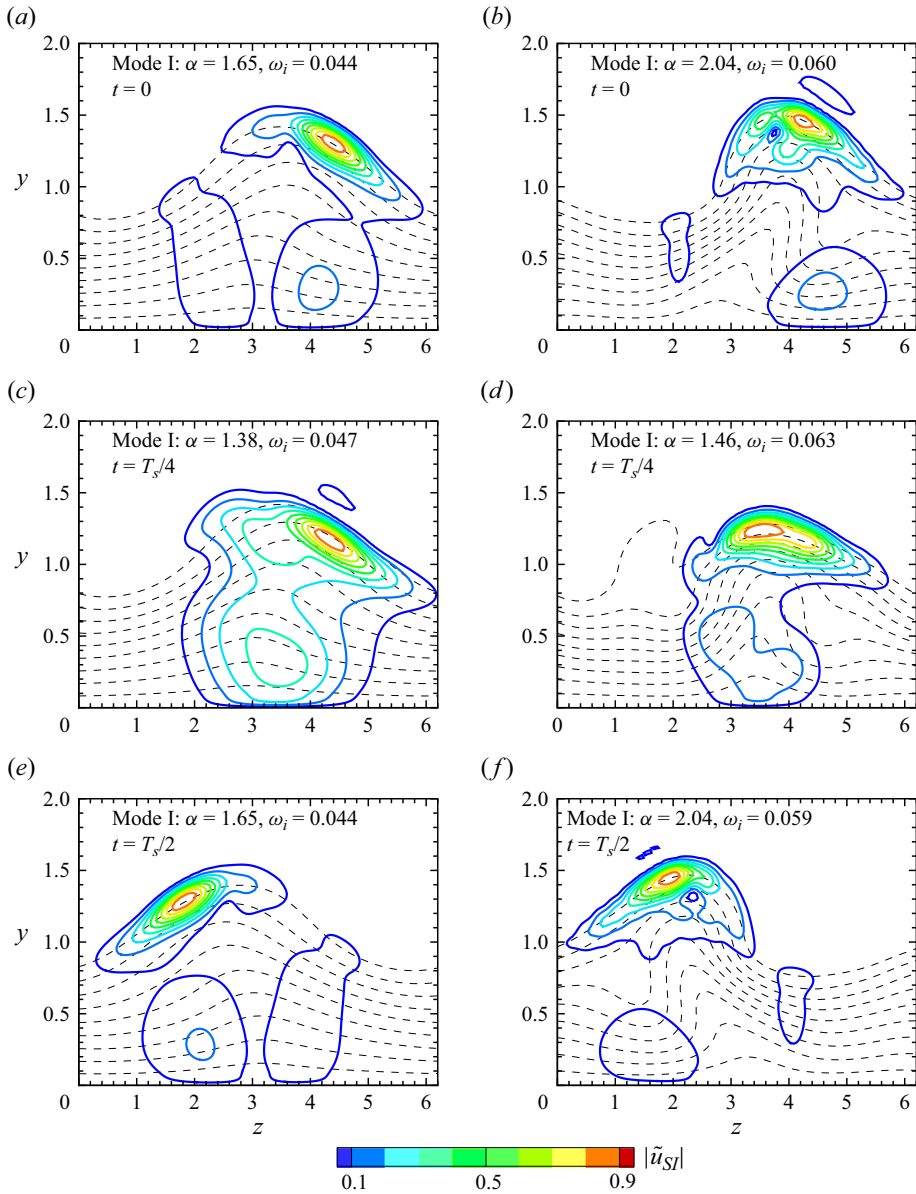


Figure 24. Eigenfunctions of $|\tilde{u}_{SJ}|$ of mode I for cases C and E at $x = 300$: (a,b) $t = 0$; (c,d) $t = T_s/4$; (e,f) $t = T_s/2$. The dashed lines represent the contours of the base flow \tilde{U}_B .

N -factor. Meanwhile, at different initial time instants, the N -factor at $x = 300$ and $\omega = 2$ for case D can vary from 5 to 11, indicating the intermittent emergence of high-amplitude perturbations.

The dependence of the N -factors on ω for $x = 240$ and 300 is summarised in figures 27(a) and 27(b), respectively, where the shaded areas represent the results for the 16 initial phases. To better quantify the impact of the wall vibration on the amplitude accumulation, we introduce

$$\Delta N(x, \bar{t}_0) = N(x, \bar{t}_0) - N_{\mathcal{E}_s=0}(x) \quad (4.5)$$

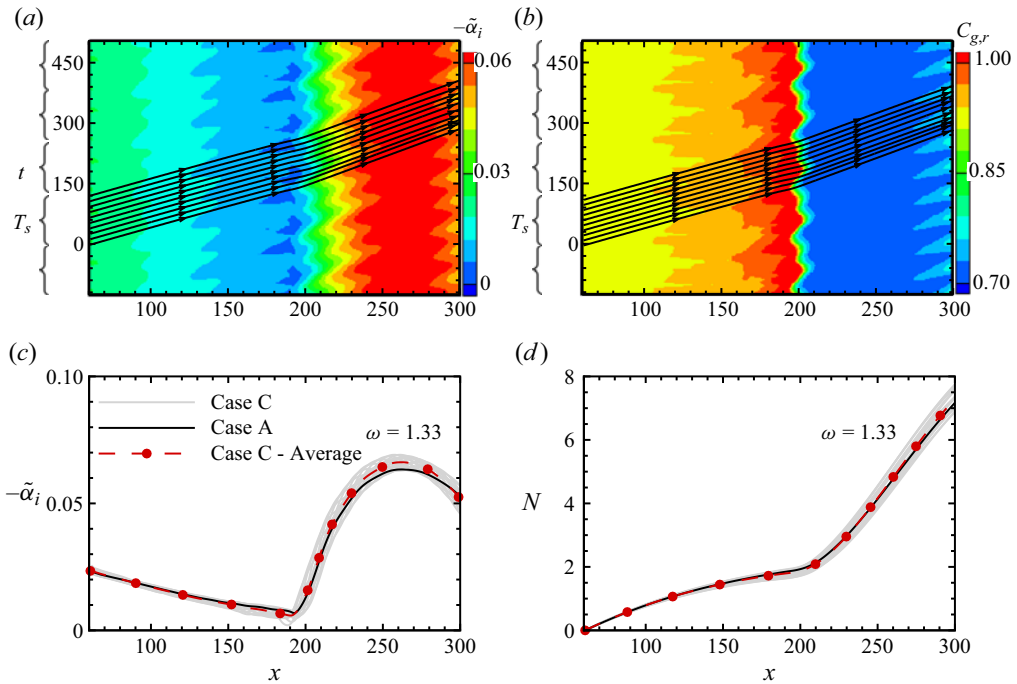


Figure 25. Contours of (a) the growth rate $-\tilde{\alpha}_i(x, t)$ and (b) the group velocity $C_{g,r}$ in the $x-t$ plane for $\omega = 1.33$ for case C. The arrowed lines denote the trajectories of the SI propagation for different initial phases. (c,d) The growth rate and the N -factor for different initial phases, respectively, where the results for their averaged value and those for case A are shown by the red and black lines, respectively.

to denote the change of the N -factor relative to the no-vibration case. The results of $\Delta N(240, \bar{t}_0)$ and $\Delta N(300, \bar{t}_0)$ are shown in figures 27(c) and 27(d), respectively. It is clearly seen that for $\omega < 1.33$, the majority of the SI perturbations are suppressed by the vibration ($\Delta N < 0$), whereas for $\omega > 1.33$, an overall enhancement is observed ($\Delta N > 0$). Additionally, the shaded areas are wider for a higher-frequency band. The implication is that although on average the perturbations are enhanced by the vibration with $\omega > 1.33$, a postponement of transition can also be observed at some time instants, showing a strong intermittent feature.

In figure 28(a), we further summarise the dependence of ΔN at $x = 300$ on initial phases for $\omega = 0.83$. The values of ΔN for both cases B and C are less than -0.18 , indicating a stabilising effect of the vibration for the relatively low-frequency SI modes. The ΔN values vary remarkably as the initial phase changes, and the averaged stabilising effect, shown by the dashed lines, is stronger when the vibration amplitude \mathcal{E}_s is larger. However, for higher frequencies, $\omega = 1.33$ or 1.67 , as shown in figures 28(b,c), an overall strong destabilising effect of the vibration is observed, except at some particular initial phases. The implication is that premature transition may appear if the high-frequency SI modes are the key factor to trigger the bypass transition.

5. Concluding remarks and discussion

For cruising high-speed vehicles, the surface vibration frequently appears as wall perturbations, which may induce an appreciative effect on the laminar–turbulent transition, leading to a remarkable change of the aerodynamic performance of the flights.

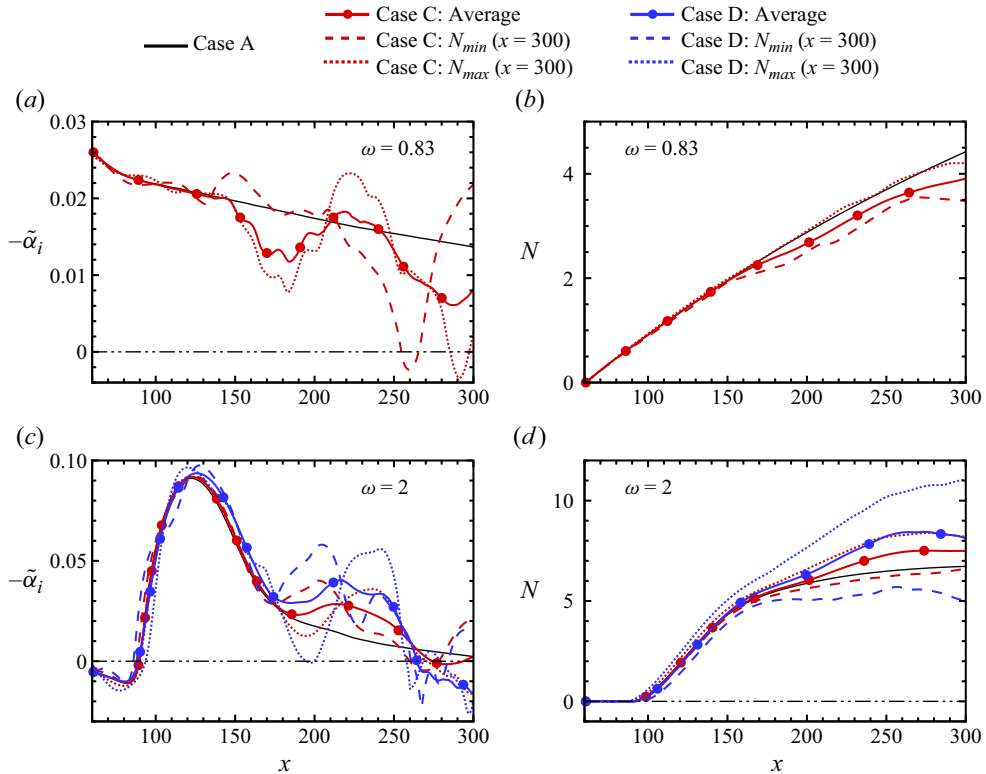


Figure 26. Streamwise evolution of (a,c) growth rate $-\tilde{\alpha}_i$ and (b,d) the N -factor of the SI modes, for (a,b) $\omega = 0.83$ and (c,d) $\omega = 2.0$. Black curves indicate case A; red curves indicate case C; blue curves indicate case D. Solid lines with circles indicate time-averaged value; dashed (dotted) lines indicate a phase where the growth rate at $x = 300$ reaches the maximum (minimum) value.

However, this mechanism is not well understood. To address this issue, in this paper we develop a novel, high-efficiency numerical approach, namely (i) calculating the entrainment of the freestream vortical disturbances (FSVDs) and the excitation of the non-modal streaks using the harmonic weakly nonlinear Navier–Stokes (HWNNS) approach to accommodate the rapid distortion of the perturbation in the leading-edge vicinity, and (ii) calculating the nonlinear evolution of the streaks in the downstream region to accommodate the nonlinear interaction of finite-amplitude Fourier modes. From comparison with the DNS results for a number of representative case studies, the HWNNS + NPSE approach (where NPSE means nonlinear parabolised stability equation) is confirmed to be reliable and accurate for calculating the evolution of boundary-layer perturbations excited by the FSVD–vibration interaction in hypersonic boundary layers.

It is found that the entrainment of low-frequency FSVDs would lead to excitation and amplification of non-modal perturbations in hypersonic boundary layers, appearing as longitudinal streaks in both the streamwise velocity and temperature components, and the temperature perturbation is much greater due to the compressibility effect. If the perturbation frequency is above a certain value, then the non-modal perturbation would evolve into the Mack first mode in a downstream position. For a higher frequency, the transition from non-modal perturbation to the Mack mode appears earlier, and at the same

Influence of wall vibration on non-modal perturbations

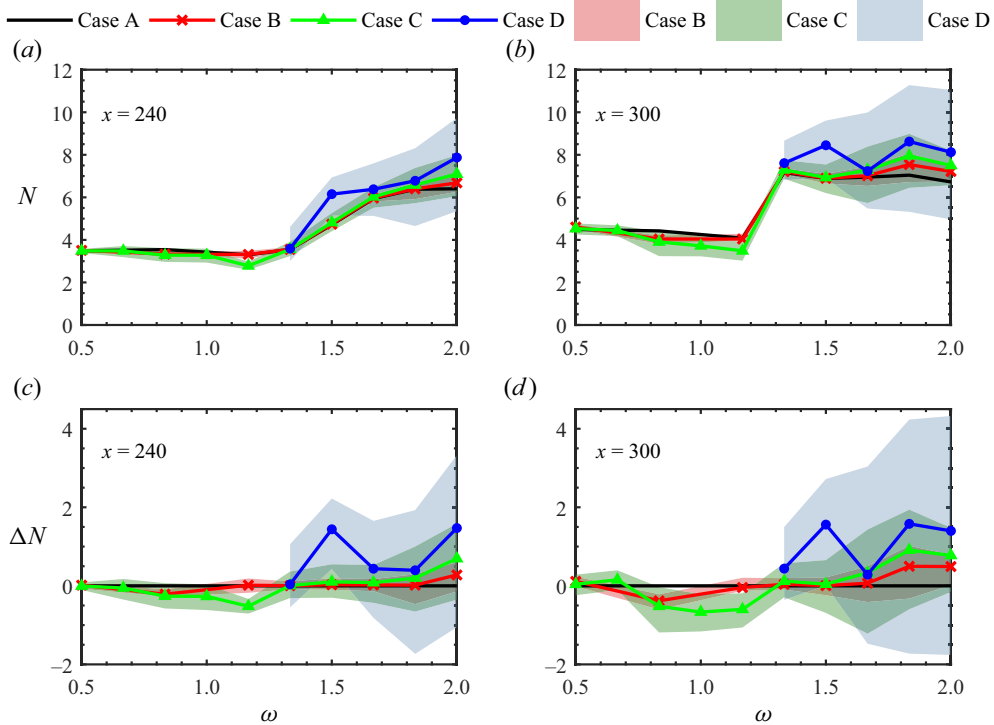


Figure 27. Dependence on ω of (a,b) the N -factor and (c,d) ΔN at $x = 240$ and 300 for cases A, B, C and D. Lines indicate time-averaged solutions; shaded areas indicate 16-instants solutions.

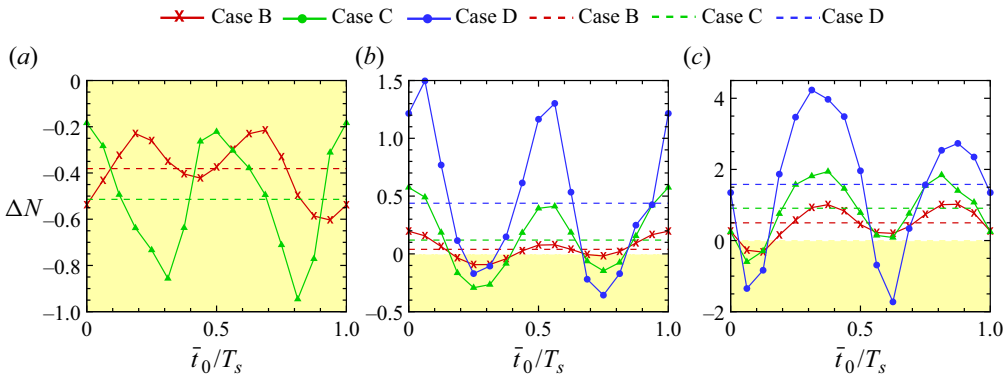


Figure 28. Dependence on \bar{t}_0/T_s of ΔN for the SI modes with (a) $\omega = 0.83$, (b) $\omega = 1.33$ and (c) $\omega = 1.83$ at $x = 300$. Lines with symbols indicate results with different initial phases; dashed lines indicate time-averaged results; yellow-shaded areas indicate $\Delta N < 0$.

position, the critical frequency distinguishing the non-modal and modal perturbations increases with the spanwise wavenumber.

When the lateral vibration is considered, the perturbations with frequencies $\omega_f \pm \omega_s$ would be excited in the boundary layer. It is found from a scaling estimate that even if the vibration amplitude is as small as R^{-1} , it would have a leading-order impact on the FSVD-induced perturbation (with frequency ω_f), because the streamwise gradient of the FSVD-induced perturbation is also of that magnitude. Therefore, the governing equations

of \tilde{u}_f and \tilde{u}_\pm form a coupled linear system, which is in principle the same as in the asymptotic study conducted by Hicks & Ricco (2015). These equations are solved using an iterative scheme. Because in each iterative step the governing equations appear as a weakly nonlinear form, the HWNNS approach is so-named. A parametric study of the response to the interaction of the FSVD and the surface vibration based on the HWNNS approach is carried out. The FSVD-induced non-modal perturbation \tilde{u}_f is suppressed by the lateral vibration, but the Mack first mode in the downstream region is enhanced. Such an effect becomes more evident as the vibration intensifies. The perturbation excited by the FSVD–vibration interaction \tilde{u}_\pm increases monotonically with the vibration amplitude. Therefore, when the vibration is relatively strong, say $\mathcal{E}_s = 0.03$, the amplitude of \tilde{u}_\pm could become comparable with that of \tilde{u}_f in a downstream location, indicating a severe distortion of the FSVD-induced streaks.

Choosing $\mathcal{E}_f = 0.0005$, the FSVD-induced streaks may accumulate to finite amplitudes in the downstream region. Therefore, the NPSE approach is employed for calculations of the nonlinear interactions among different Fourier modes. The NPSE calculations start from $x = 60$, where the nonlinearity is rather weak, and the inflow perturbations are obtained by the HWNNS calculations. The lateral vibration induces a Stokes layer of the spanwise velocity perturbation, which distorts the FSVD-induced streaks remarkably if the vibration intensity is moderate. Performing the secondary instability (SI) analysis, it is found that the instability property of the streaky base flow depends strongly on time, and the SI modes may be promoted or suppressed depending on their initial phases. Overall, the averaged effect is that the low-frequency and high-frequency SI modes are stabilised and destabilised by the vibration, respectively. Integrating the growth rates along the streamwise direction, we find that the high-frequency SI modes can be amplified by a greater factor, indicating their dominant role in triggering the bypass transition to turbulence. Therefore, the vibration is likely to promote the bypass transition for our cases, and a stronger vibration enhances the promotion effect.

It should be noted that our observation is a little different from the incompressible configurations studied by Hack & Zaki (2014), for which a severe suppression of the non-modal streaks is observed for the properly chosen parameter set. This may be attributed to the following reason. The dimensionless amplitude of the vibration velocity for incompressible boundary layers could reach magnitudes of $O(0.1)$, but such values are unrealistic for a hypersonic configuration. In the case of weak vibrations with $\mathcal{E}_s = O(0.01)$, the suppression effect of the FSVD-induced streaks with frequency ω_f is limited. However, the vibration induces an additional perturbation with a different frequency $\omega_f \pm \omega_s$, which has the potential to be amplified to the nonlinear phase in the downstream region. Indeed, whether the SI of the streaks is enhanced or suppressed depends on the combined effect of the aforementioned two factors.

Actually, for hypersonic flights, the flat-plate model with a sharp leading edge studied in this paper is only idealised, and a blunt leading edge is usually employed to avoid extreme heat load. In such situations, the bow-shaped leading-edge shock appears, and the numerical scheme for the HLNS/HWNNS approach employed in this paper is not adequate to deal with the sharp jump of perturbations. Thus future work may be directed to the development of the shock-fitting scheme for the HLNS/HWNNS approach, to cope with the hypersonic transition for more complex geometries. Nevertheless, the present paper is still a significant step for developing an efficient means for the study of hypersonic transition.

Funding. This work is supported by the National Science Foundation of China (grant nos U20B2003, 92371104, 12372222, 12002235 and 11988102) and the Strategic Priority Research Program, CAS (no. XDB22040104).

Influence of wall vibration on non-modal perturbations

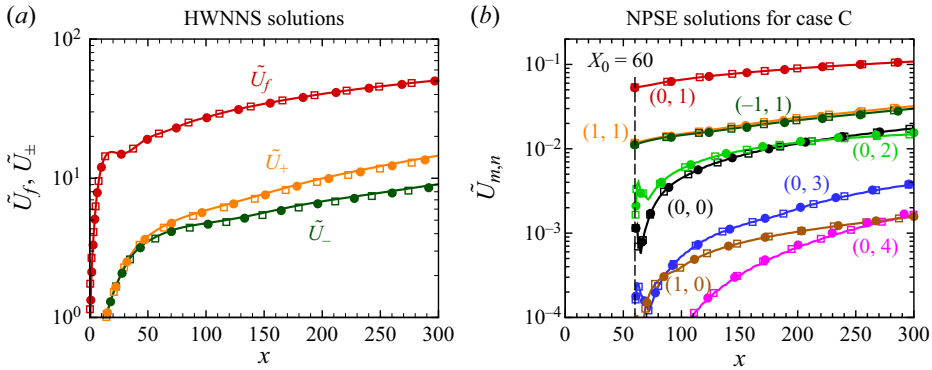


Figure 29. Resolution studies for HWNNS and NPSE obtained by different mesh scales. Lines indicate the standard mesh; squares indicate the mesh refined in the x -direction; circles indicate the mesh refined in the y -direction.

Declaration of interests. The authors report no conflict of interest.

Author ORCIDs.

- Qinyang Song <https://orcid.org/0000-0002-7668-9954>;
- Ming Dong <https://orcid.org/0000-0003-3408-8613>;
- Lei Zhao <https://orcid.org/0000-0003-0101-4845>.

Appendix A. Resolution studies for HWNNS and NPSE

In figures 29(a) and 29(b), we show the resolution studies for the HWNNS and NPSE approaches, respectively, where $\omega_f = 0$, $k_3 = 1$, $\Theta = 45^\circ$ and $\omega_s = 0.05$. For the NPSE calculation, the amplitudes of the FSVD and vibration are chosen from case C. The results for three mesh scales are compared, where the standard mesh includes 401×301 for the HWNNS approach and 230×301 for the NPSE, and the other two mesh scales include doubled grid points in the x - and y -directions, respectively. Perfect agreement is achieved, confirming the reliability of our calculations.

Appendix B. Verification of HWNNS and NPSE calculations by DNS

As a newly-developed approach combining the HWNNS and NPSE approaches, the central issue is to confirm its reliability and accuracy by the well-accepted tool (DNS). The DNS code is the same as that used in § 2.3, but we need to introduce a low-frequency FSVD at both the inlet and upper boundaries and a lateral vibration at the wall, and extend the calculations to be 3-D; the detailed introduction of the DNS approach can be found in Song, Zhao & Huang (2020) and Song *et al.* (2023a).

The first group of case studies for verification is selected by putting the amplitude of FSVDs to be small, $\mathcal{E}_f = 10^{-8}$, for which the high-order harmonics in (2.3) are indeed negligible. For these cases, the DNS results can be compared directly to the HWNNS calculations. Figures 30(a) and 30(b) display the streamwise evolution of the amplitude of \tilde{U}_f and \tilde{U}_\pm for $\mathcal{E}_s = 0.0001$ and 0.01, respectively, and the perturbation profiles at representative x locations are shown in figures 30(c–h). Although a slight discrepancy appears for \tilde{u}_\pm in the downstream locations, the overall agreement between the results obtained by the two approaches is quite satisfactory.

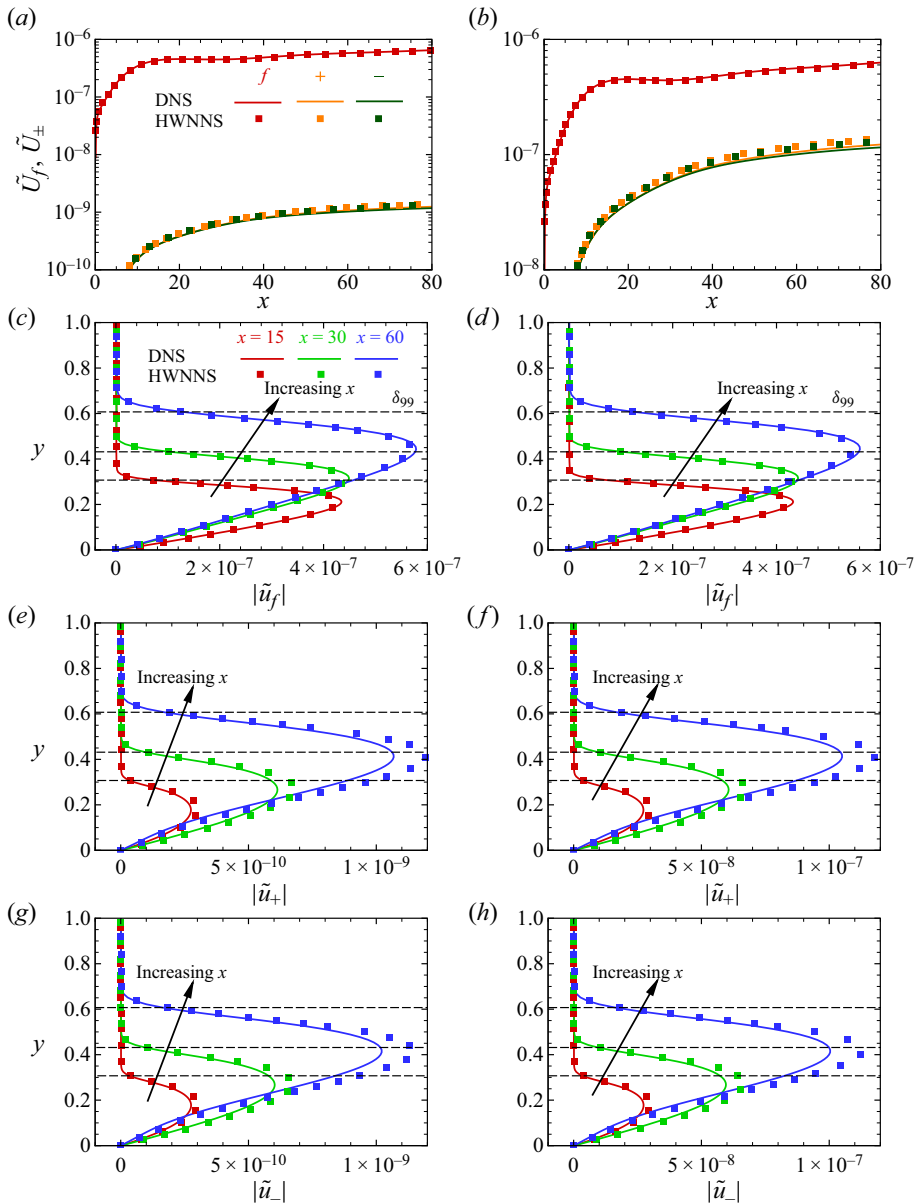


Figure 30. Comparison of the evolution of perturbations between HWNNS and DNS for $\mathcal{E}_f = 10^{-8}$, where $\omega_f = 0$, $k_3 = 1$ and $\Theta = 15^\circ$, for (a,c,e,g) $\mathcal{E}_s = 0.0001$, (b,d,f,h) $\mathcal{E}_s = 0.01$. (a,b) Streamwise evolution of \tilde{U}_f and \tilde{U}_\pm . (c–h) Wall-normal profiles at $x = 15, 30$ and 60 , in which the horizontal dashed lines denote the nominal boundary-layer thickness.

In figure 31, we show the results by increasing the FSVD amplitude to $\mathcal{E}_f = 0.0005$, and the parameters are chosen from cases C and E. It needs to be emphasised that for a clean comparison, only one Fourier component in (4.1), $\mathcal{E}_f \hat{\phi}_{f,+} \exp(i(k_2 y + k_3 z)) + c.c.$, is considered here. Therefore, the numerical results in this figure are different from the NPSE calculations in figure 16. Although the HWNNS calculations for \tilde{u}_f (or $\tilde{U}_{0,1}$) and \tilde{u}_\pm (or $\tilde{U}_{\pm,1,1}$) agree overall with the DNS results with a limited discrepancy, they do

Influence of wall vibration on non-modal perturbations

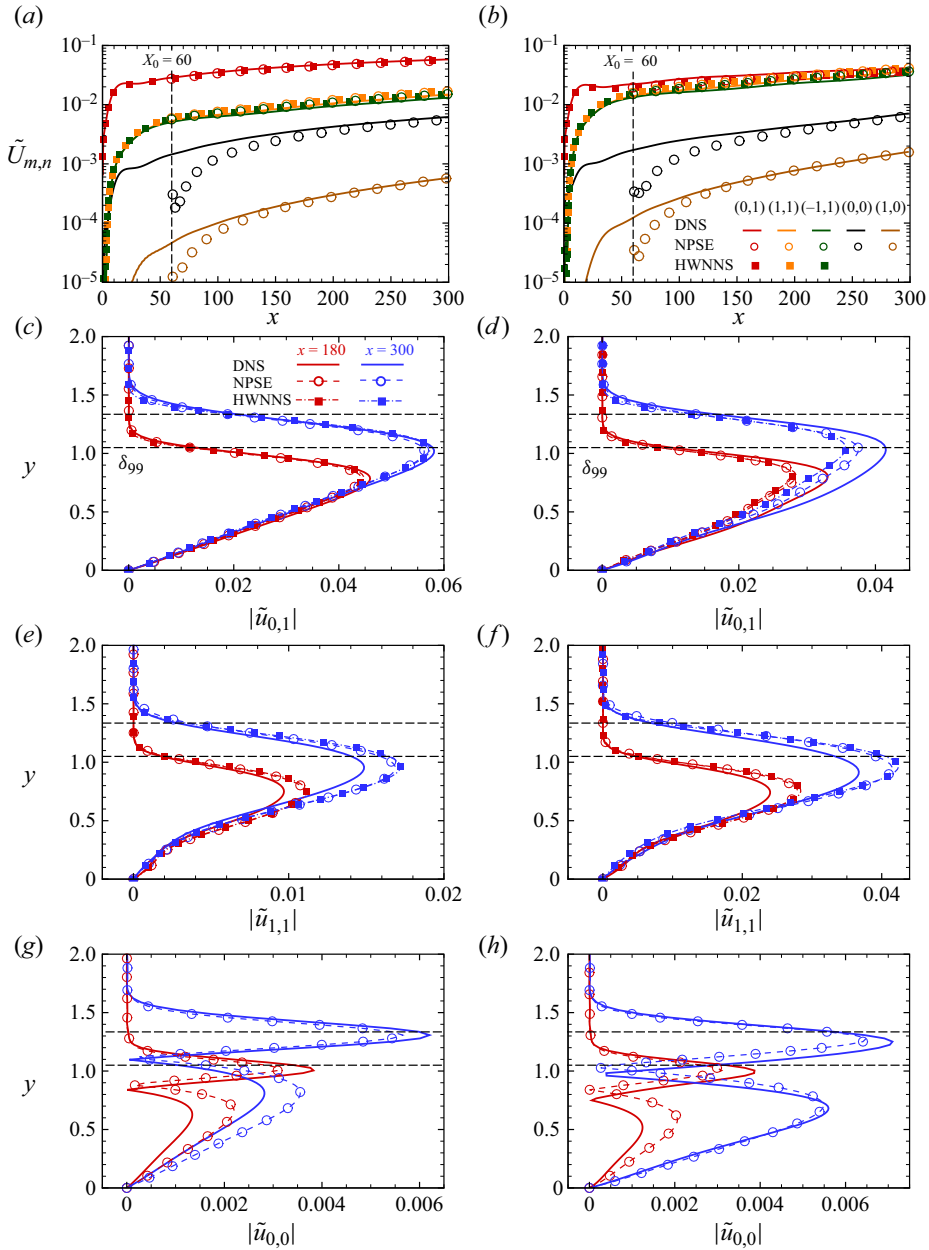


Figure 31. Comparison of the evolution of perturbations between HWNNS, NPSE and DNS for (a,c,e,g) case C, and (b,d,f,h) case E. (a,b) Streamwise evolution of $\tilde{U}_{m,n}$. (c–h) Wall-normal profiles at $x = 180$ and 300 , in which the horizontal dashed lines denote the nominal boundary-layer thickness.

not include the evolution of the MFD, component (0, 0), and the harmonics shown by the black and brown curves in the DNS results. Since the MFD has reached amplitude 0.006 at $x = 300$ for both cases, its impact on the SI would not be neglected. Therefore, the NPSE calculation is employed to take into account the nonlinear interaction among different Fourier components, starting from $x = 60$. After a short adjustment ($x \in (60, 100)$), the

agreement between the NPSE and DNS results is quite satisfactory. Additionally, as expected, the NPSE calculations of $\tilde{U}_{0,1}$ and $\tilde{U}_{\pm 1,1}$ are a little closer to the DNS results in comparison with the HWNNS calculations in downstream regions.

To conclude, the above comparison confirms that our HWNNS + NPSE approach provides reliable and accurate results in comparison with those obtained by DNS, although there exists a small discrepancy in the downstream region for both low and high \mathcal{E}_f values. The reason may be attributed to the difference between the numerical schemes, i.e. the central scheme is employed for HWNNS, and the flux-splitting method with the WENO scheme is employed for DNS. The existence of the sharp leading edge challenges the numerical approach, and a small discrepancy computed by different numerical schemes may occur in the leading-edge vicinity, which will not be diminished by increasing the grid resolution. Such a discrepancy may be removed if the sharp leading edge is replaced by a blunt leading edge, which will be considered in our future study.

REFERENCES

- ANDERSSON, P., BRANDT, L., BOTTARO, A. & HENNINGSON, D.S. 2001 On the breakdown of boundary layer streaks. *J. Fluid Mech.* **428**, 29–60.
- CHANG, C.L. & MALIK, M.R. 1994 Oblique-mode breakdown and secondary instability in supersonic boundary layers. *J. Fluid Mech.* **273**, 323–360.
- DONG, M., LIU, Y. & WU, X. 2020 Receptivity of inviscid modes in supersonic boundary layers due to scattering of free-stream sound by localised wall roughness. *J. Fluid Mech.* **896**, A23.
- DONG, M. & ZHAO, L. 2021 An asymptotic theory of the roughness impact on inviscid Mack modes in supersonic/hypersonic boundary layers. *J. Fluid Mech.* **913**, A22.
- FEDOROV, A.V. & KHOKHLOV, A.P. 2001 Prehistory of instability in a hypersonic boundary layer. *Theor. Comput. Fluid Dyn.* **14**, 359–375.
- GASTER, M. 1962 A note on the relation between temporally-increasing and spatially-increasing disturbances in hydrodynamic stability. *J. Fluid Mech.* **14** (2), 222–224.
- GOLDSTEIN, M.E. & RICCO, P. 2018 Non-localized boundary layer instabilities resulting from leading edge receptivity at moderate supersonic Mach numbers. *J. Fluid Mech.* **838**, 435–477.
- GOPINATH, A. & JAMESON, A. 2005 Time spectral method for periodic unsteady computations over two- and three-dimensional bodies. In *43rd AIAA Aerospace Sciences Meeting and Exhibit*, AIAA Paper 2005-1220.
- GOPINATH, A. & JAMESON, A. 2006 Application of the time spectral method to periodic unsteady vortex shedding. In *44th AIAA Aerospace Sciences Meeting and Exhibit*, AIAA Paper 2006-449.
- HACK, M.P. & ZAKI, T.A. 2014 The influence of harmonic wall motion on transitional boundary layers. *J. Fluid Mech.* **760**, 63–94.
- HACK, M.P. & ZAKI, T.A. 2015 Modal and non-modal stability of boundary layers forced by spanwise wall oscillations. *J. Fluid Mech.* **778**, 389–427.
- HADER, C. & FASEL, H.F. 2019 Direct numerical simulations of hypersonic boundary-layer transition for a flared cone: fundamental breakdown. *J. Fluid Mech.* **869**, 341–384.
- HAN, L., YUAN, J., DONG, M. & FAN, Z. 2021 Secondary instability of the spike–bubble structures induced by nonlinear Rayleigh–Taylor instability with a diffuse interface. *Phys. Rev. E* **104** (3), 035108.
- HERNÁNDEZ, C.G. & WU, X. 2019 Receptivity of supersonic boundary layers over smooth and wavy surfaces to impinging slow acoustic waves. *J. Fluid Mech.* **872**, 849–888.
- HICKS, P.D. & RICCO, P. 2015 Laminar streak growth above a spanwise oscillating wall. *J. Fluid Mech.* **768**, 348–374.
- JIANG, G.S. & SHU, C.W. 1996 Efficient implementation of weighted ENO schemes. *J. Comput. Phys.* **126** (1), 202–228.
- JUNG, W.J., MANGIACACCHI, N. & AKHAVAN, R. 1992 Suppression of turbulence in wall-bounded flows by high-frequency spanwise oscillations. *Phys. Fluids A* **4** (8), 1605–1607.
- KACHANOV, Y.S. 1994 Physical mechanisms of laminar–boundary-layer transition. *Annu. Rev. Fluid Mech.* **26** (1), 411–482.
- LEIB, S., WUNDROW, D.W. & GOLDSTEIN, M. 1999 Effect of free-stream turbulence and other vortical disturbances on a laminar boundary layer. *J. Fluid Mech.* **380**, 169–203.
- MACK, L.M. 1987 Review of linear compressible stability theory. In *Stability of Time Dependent and Spatially Varying Flows* (ed. D.L. Dwoyer & M.Y. Hussaini), pp. 164–187. Springer.

Influence of wall vibration on non-modal perturbations

- MARENSE, E., RICCO, P. & WU, X. 2017 Nonlinear unsteady streaks engendered by the interaction of free-stream vorticity with a compressible boundary layer. *J. Fluid Mech.* **817**, 80–121.
- NAGARAJAN, S., LELE, S. & FERZIGER, J. 2007 Leading-edge effects in bypass transition. *J. Fluid Mech.* **572**, 471–504.
- NEGI, P.S., MISHRA, M., SCHLATTER, P. & SKOTE, M. 2019 Bypass transition delay using oscillations of spanwise wall velocity. *Phys. Rev. Fluids* **4**, 063904.
- NIU, M. & SU, C. 2023 Receptivity and its influence on transition prediction of a hypersonic boundary layer over a small bluntness cone. *Phys. Fluids* **35** (3), 034109.
- OVCHINNIKOV, V., CHOUDHARI, M.M. & PIOMELLI, U. 2008 Numerical simulations of boundary-layer bypass transition due to high-amplitude free-stream turbulence. *J. Fluid Mech.* **613**, 135–169.
- PARÉDES, P., CHOUDHARI, M.M., LI, F., JEWELL, J.S. & KIMMEL, R.L. 2019a Nonmodal growth of traveling waves on blunt cones at hypersonic speeds. *AIAA J.* **57** (11), 4738–4749.
- PARÉDES, P., CHOUDHARI, M.M., LI, F., JEWELL, J.S., KIMMEL, R.L., MARINEAU, E.C. & GROSSIR, G. 2019b Nose-tip bluntness effects on transition at hypersonic speeds. *J. Spacecr. Rockets* **56** (2), 369–387.
- QIN, F. & WU, X. 2016 Response and receptivity of the hypersonic boundary layer past a wedge to free-stream acoustic, vortical and entropy disturbances. *J. Fluid Mech.* **797**, 874–915.
- QUINTANILHA, H., PARÉDES, P., HANIFI, A. & THEOFILIS, V. 2022 Transient growth analysis of hypersonic flow over an elliptic cone. *J. Fluid Mech.* **935**, A40.
- REN, J. & FU, S. 2015 Secondary instabilities of Görtler vortices in high-speed boundary layer flows. *J. Fluid Mech.* **781**, 388–421.
- RICCO, P. 2011 Laminar streaks with spanwise wall forcing. *Phys. Fluids* **23** (6), 064103.
- RICCO, P., LUO, J. & WU, X. 2011 Evolution and instability of unsteady nonlinear streaks generated by free-stream vortical disturbances. *J. Fluid Mech.* **677**, 1–38.
- RICCO, P., SKOTE, M. & LESCHZINER, M.A. 2021 A review of turbulent skin-friction drag reduction by near-wall transverse forcing. *Prog. Aerosp. Sci.* **123**, 100713.
- RICCO, P. & WU, X. 2007 Response of a compressible laminar boundary layer to free-stream vortical disturbances. *J. Fluid Mech.* **587**, 97–138.
- SMITH, A.M.O. 1956 Transition, pressure gradient and stability theory. In *IX International Congress of Applied Mechanics* (ed. I.A.H. Hult & F.A. McClintock). University of Brussels.
- SONG, Q., ZHAO, L. & DONG, M. 2023a Effect of porous coatings on the nonlinear evolution of Mack modes in hypersonic boundary layers. *Phys. Fluids* **35** (5), 054115.
- SONG, R., DONG, M. & ZHAO, L. 2023b Effect of cone rotation on the nonlinear evolution of Mack modes in supersonic boundary layers. *J. Fluid Mech.* **971**, A4.
- SONG, R., DONG, M. & ZHAO, L. 2024 Principle of fundamental resonance in hypersonic boundary layers: an asymptotic viewpoint. *J. Fluid Mech.* **978**, A30.
- SONG, R., ZHAO, L. & HUANG, Z. 2020 Secondary instability of stationary Görtler vortices originating from first/second Mack mode. *Phys. Fluids* **32** (3), 034109.
- TOUBER, E. & LESCHZINER, M.A. 2012 Near-wall streak modification by spanwise oscillatory wall motion and drag-reduction mechanisms. *J. Fluid Mech.* **693**, 150–200.
- WAN, B., SU, C. & CHEN, J. 2020 Receptivity of a hypersonic blunt cone: role of disturbances in entropy layer. *AIAA J.* **58** (9), 4047–4054.
- WU, X. 2019 Nonlinear theories for shear flow instabilities: physical insights and practical implications. *Annu. Rev. Fluid Mech.* **51**, 451–485.
- WU, X. 2023 New insights into turbulent spots. *Annu. Rev. Fluid Mech.* **55** (1), 45–75.
- WU, X. & DONG, M. 2016 Entrainment of short-wavelength free-stream vortical disturbances in compressible and incompressible boundary layers. *J. Fluid Mech.* **797**, 683–728.
- WU, X., MOIN, P. & HICKEY, J.P. 2014 Boundary layer bypass transition. *Phys. Fluids* **26** (9), 091104.
- XU, D., LIU, J. & WU, X. 2020 Görtler vortices and streaks in boundary layer subject to pressure gradient: excitation by free stream vortical disturbances, nonlinear evolution and secondary instability. *J. Fluid Mech.* **900**, A15.
- XU, D., ZHANG, Y. & WU, X. 2017 Nonlinear evolution and secondary instability of steady and unsteady Görtler vortices induced by free-stream vortical disturbances. *J. Fluid Mech.* **829**, 681–730.
- XU, J., LIU, J., ZHANG, Z. & WU, X. 2023 Spatial-temporal transformation for primary and secondary instabilities in weakly non-parallel shear flows. *J. Fluid Mech.* **959**, A21.
- ZHANG, A., DONG, M. & ZHANG, Y. 2018 Receptivity of secondary instability modes in streaky boundary layers. *Phys. Fluids* **30** (11), 114102.
- ZHAO, L. & DONG, M. 2022 Effect of surface temperature strips on the evolution of supersonic and hypersonic Mack modes: asymptotic theory and numerical results. *Phys. Rev. Fluids* **7**, 053901.

- ZHAO, L., DONG, M. & YANG, Y. 2019 Harmonic linearized Navier–Stokes equation on describing the effect of surface roughness on hypersonic boundary-layer transition. *Phys. Fluids* **31** (3), 034108.
- ZHAO, L., HE, J. & DONG, M. 2023 Asymptotic theory of Mack-mode receptivity in hypersonic boundary layers due to interaction of a heating/cooling source and a freestream sound wave. *J. Fluid Mech.* **963**, A34.
- ZHAO, L., ZHANG, C., LIU, J. & LUO, J. 2016 Improved algorithm for solving nonlinear parabolized stability equations. *Chin. Phys. B* **25** (8), 084701.
- ZHONG, X. & WANG, X. 2012 Direct numerical simulation on the receptivity, instability, and transition of hypersonic boundary layers. *Annu. Rev. Fluid Mech.* **44** (1), 527–561.